

1 *This paper is a non-peer reviewed preprint submitted to EarthArXiv*

2 DOI:<https://doi.org/10.31223/X5T407>

3
4 **Title:**

5 **Inferring Long-Term Tectonic Uplift Patterns from Bayesian Inversion of Fluvially-Incised**
6 **Landscapes**

7
8 **Bar Oryan^{1*}, Boris Gailleton², Jean-Arthur Olive³, Luca C. Malatesta⁴ and Romain Jolivet^{3,5}**

9
10 **Affiliations:**

11 (1)Scripps Institution of Oceanography, UC San Diego, La Jolla, CA 92093,USA

12 (2)Univ. Rennes, Géosciences Rennes, UMR 6118, 35000 Rennes, France.

13 (3)Laboratoire de Géologie, École normale supérieure – PSL, CNRS UMR 8538, Paris, France.

14 (4)Earth Surface Process Modelling, GFZ German Research Center for Geosciences, Potsdam,
15 Germany.

16 (5)Institut Universitaire de France, 1 rue Descartes, 75006 Paris.

17

18 Corresponding author email:

19 Bar Oryan - Bar.oryan@columbia.edu

20 **Abstract**

21 Earth surface processes encode the combined forcing of tectonics and climate in
22 topography. Separating their contributions is essential for using landscapes as quantitative
23 records of crustal deformation. Here, we develop a method for inverting fields of long-term rock
24 uplift from fluvially-incised landscapes, while accounting for spatial variability in climatic
25 conditions and rock erodibility. Our approach operates in the χ -space reference frame and
26 handles spatial variability in key geomorphological parameters using B-spline interpolating
27 functions. Through inversions of 170 synthetic landscapes, we demonstrate that our method
28 accurately captures spatial variations in landscape properties, even when applied to settings that
29 deviate from the ideal model of equilibrated detachment-limited channels, which underpins the
30 χ -space framework. Consequently, we apply our inversion to five natural landscapes shaped by
31 normal faults (half-grabens), and to a 200 km wide region of the Himalayas. We show that our
32 inversion can resolve the effect of climate and lithology while extracting uplift fields that are
33 consistent with patterns expected from upper crustal flexure and previous estimates of uplift
34 derived from geomorphological markers. The success of our method in recovering uplift patterns,
35 isolated from the effects of climate and erodibility, highlights its applicability to settings where
36 long-term uplift trends are unknown, paving the path to deciphering time-averaged tectonic
37 fingerprints recorded in landscapes over tens of thousands of years.

38

39

40

41

42 **Plain Language Summary**

43 Earth's topography is uniquely shaped by both deep tectonic activity and the erosive processes
44 that sculpt its surface. Utilizing these landscapes to deduce tectonic activity presents valuable
45 insights, albeit elusive. In this study, we introduce a mathematical inversion method utilizing
46 geomorphic indices to extract tectonic uplift patterns from landscapes. We assess this method's
47 effectiveness on simulated synthetic landscapes that include a variety of surface processes. Our
48 findings confirm that the method can accurately retrieve uplift rate patterns, even in landscapes
49 not solely governed by steady state detachment-limited erosion—the assumption underlying our
50 inversion technique. Applying this method to natural landscapes shaped by normal faults and the
51 Himalayas, we demonstrate that our extracted uplift patterns align with expected patterns of
52 tectonic warping. This approach sets the stage for using landscapes to decipher tectonic signals
53 accumulated over tens of thousands of years.

54

55 **Key Points**

- 56 • New method infers unknown uplift patterns and variable erodibility from fluvial
57 landscapes using a Bayesian approach.
- 58 • Synthetic tests reveal the broad applicability of our methods, even in systems that deviate
59 from the steady-state detachment-limited incision assumption.
- 60 • Inverting six natural landscapes yields uplift fields consistent with previous uplift
61 estimates and crustal flexure.

62

63 1 Introduction

64 Earth's topography reflects a delicate balance between internal tectonic forcings and
65 climate-modulated surface processes. The first induce vertical motion of the surface through
66 processes such as faulting, dynamic topography and isostasy (e.g., Faccenna et al., 2019; King et
67 al., 1988; Watts, 2001) while the latter level relief by eroding bedrock and transporting/
68 depositing the resulting sediments (e.g., Merritt et al., 2003). Thus, the shape of landscapes
69 represents a snapshot of the ever-evolving competition of these two processes (Kirby & Whipple,
70 2012; Molnar & England, 1990; Willgoose et al., 1991).

71 Disentangling the contributions of surface processes and tectonic forces is crucial for
72 deriving insights into tectonic activities, which is a core goal of tectonic geomorphology (e.g.,
73 Armijo et al., 1996; Lavé & Avouac, 2001; Malatesta et al., 2021). Extracting spatial patterns of
74 rock uplift rates from landscapes is particularly important as it provides direct quantitative
75 constraints on the underlying tectonic mechanisms. For instance, in landscapes shaped by normal
76 faults, spatially-varying vertical rock uplift are used to estimate the effective elastic thickness of
77 the lithosphere (Armijo et al., 1996). The shape of uplift recorded around fault scarps offers
78 insights into the slip behavior of the fault (e.g, Holtmann et al., 2023). Perhaps even more
79 critically, variations in rock uplift rates across subduction zone forearcs may be used to infer the
80 pattern of interseismic locking on the megathrust. This is because the latter modulates the
81 accumulation of inelastic strain over multiple seismic cycles, which is ultimately encoded in
82 forearc landscapes (e.g., Cattin & Avouac, 2000; Jolivet et al., 2020; Malatesta et al., 2021;
83 Meade, 2010; Oryan et al., 2024; Dublanchet & Olive, 2024) .

84 Nonetheless, extracting uplift fields from landscapes is challenging especially in the absence of
85 thermochronological data or geomorphological markers. Current approaches (Castillo et al.,
86 2014; Densmore et al., 2007; Ponza et al., 2010; Su et al., 2017) rely on the stream power incision
87 model (Howard & Kirby, 1983) utilizing a landscape metric called the steepness index, k_{sn} (Wobus
88 et al., 2006, See section 2 for definition). While useful, k_{sn} expresses the ratio of rock erodibility
89 to rock uplift and may be strongly skewed by unconstrained spatial variations in rock erodibility.
90 Furthermore, it depends on point measurements of surface slopes, which can be noisy (Boris
91 Gailleton et al., 2021). The χ metric, which integrates upstream changes in drainage area

92 normalized by the concavity index across entire river networks, provides a quantitative
93 alternative to recover spatial variations in uplift rates from landscapes (Perron & Royden, 2013).
94 Previous work has employed the χ metric for landscape inversion focusing on uplift rate history,
95 while neglecting or prescribing variations in uplift shape (Croissant & Braun, 2014; Fox et al.,
96 2014; L. Goren et al., 2014; Liran Goren et al., 2022; Pritchard et al., 2009; Smith et al.,
97 2024).

98 Here we extend the χ coordinate framework and invert landscapes for an unknown
99 (steady) field of rock uplift rate and variable spatial erodibility. To that end, we utilize a Bayesian
100 quasi-Newton inversion scheme which optimizes uplift shapes parameterized by B-spline
101 interpolation functions in a manner that minimizes the misfit between measured and inverted
102 elevation. We test the strengths and limitations of our method using synthetic landscapes and
103 demonstrate its ability to recover uplift shapes and erodibility coefficients while accounting for
104 climatic effects. Subsequently, we apply our method to six natural landscapes shaped by
105 divergent and convergent tectonics to demonstrate its effectiveness in real-world scenarios.

106

107 2 Inferring tectonic uplift from landscapes within the stream power 108 framework

109 2.1 The detachment-limited stream power model

110 The stream power incision model posits that the erosion rate of a riverbed at a certain
111 point is linked to water flux (captured by proxy with drainage area A), channel slope ($\frac{dz}{dx}$) and the
112 erodibility of the material (K) (Hack, 1973; Howard & Kerby, 1983). To maintain a uniform rate of
113 erosion, the river gradient diminishes downstream as drainage area increases, resulting in a
114 familiar concave river profile. According to this model, the change in elevation over time t , of a
115 river eroding at rate, E , under rock uplift, U , is described as follows:

116

117
$$1. \frac{\partial z(x,y,t)}{\partial t} = U(x, y, t) - E(x, y, t) = U(x, y, t) - K(x, y, t)A(x, y, t)^m \left(\frac{\partial z}{\partial x}\right)^n$$

118

119

120 Where m and n are constants, (x,y) is position, hereafter denoted as \vec{x} for concision.

121 The velocity at which a change in uplift rate travels upstream as a knickpoint is linked to local
122 erodibility, drainage area and topographic gradient (Rosenbloom & Anderson, 1994; Whipple &
123 Tucker, 1999):

124

125
$$2. \quad c(\vec{x}) = k(\vec{x})A(\vec{x}) \left(\frac{dz(\vec{x})}{dx} \right)^{n-1}$$

126 The time for a perturbation to travel from the river base upstream to point x_s is defined as follows
127 (Whipple & Tucker, 1999):

128

129
$$3. \quad \tau(x_s) = \int_0^{x_s} \frac{dx}{c(\vec{x})} = \int_0^{x_s} \frac{dx}{k(\vec{x})A(\vec{x})\left(\frac{dz(\vec{x})}{dx}\right)^{n-1}}$$

130

131 When erosion and uplift rates are balanced, the steady-state equation describes the equilibrium
132 slope of the river with an inverse power-law relationship between channel slope and drainage
133 area:

134

135
$$4. \quad \frac{dz}{dx} = k_{sn}A(\vec{x})^{-\frac{m}{n}}$$

136

137 Where $k_{sn} = \left(\frac{U(\vec{x})}{K(\vec{x})} \right)^{\frac{1}{n}}$ a quantity often normalized with respect to regional concavity value,
138 $\theta_{ref}(= \frac{m}{n})$ and introduced as k_{sn} which is used as a proxy of uplift to erosion ratio.

139

140 2.2 The integral approach: river profiles in χ -space

141

142 Upstream integration of equation 4 from an arbitrary base level x_b results in (Perron &
143 Royden, 2013):

144
$$5. \quad z(\vec{x}) = z(x_b) + a_s \cdot \chi(\vec{x})$$

145 Where,

146 6. $\chi = \int_{x_b}^x \frac{dx}{A^*(\vec{x})^{\frac{m}{n}}}; a_s = \left(\frac{U_0}{K_0 A_o^m}\right)^{\frac{1}{n}}$

147 and A_o is a constant reference drainage area such that $A^*(x) = \frac{A(x)}{A_o}$ is dimensionless. The

148 integral along x here denotes an upstream path a connected network of tributaries.

149 This coordinate transformation allows us to describe river profiles in terms of χ and z . In
 150 the case of spatially uniform U and K , stream profiles in χ -space will exhibit a linear relationship
 151 between the two variables, characterized by a slope a_s . In landscapes where erodibility and uplift
 152 vary spatially, the definition of χ can be amended as (Olive et al., 2022; Perron & Royden, 2013)
 153 :

154

155 7. $\chi_{u,k} = \int_{x_b}^x \left(\frac{U^*(\vec{x})}{A^*(\vec{x})^m K^*(\vec{x})} \right)^{\frac{1}{n}} dx ; a_s = \left(\frac{U_0}{K_0 A_o^m}\right)^{\frac{1}{n}}$

156

157 In this case, U_0 and K_0 are reference values so the trailing terms are dimensionless ($U^* = \frac{U}{U_0}$,
 158 $K^* = \frac{K}{K_0}$). $\chi_{u,k}$ denotes a version of χ corrected for known spatial variations in uplift rate and
 159 erodibility. If $U^*(\vec{x})$ and $K^*(\vec{x})$ are properly accounted for, the steady state landscape should verify
 160 equation (5): elevation should be linearly correlated with $\chi_{u,k}$.

161

162 3 Inverting uplift shapes from river incised landscapes

163 3.1 Forward model

164 3.1.1 Parameter space, data space and cost function

165

166 The detachment-limited stream power model in χ -space provides a robust framework to
 167 invert uplift shape from river incised landscapes. Let us begin by outlining the direct (forward)
 168 problem of river profiles in χ -space, from knowledge of the parameters $m, n, a_s, U^*(\vec{x})$ and
 169 $K^*(\vec{x})$. This is done by computing $\chi_{u,k}$ (eq. 7), and modeled river elevation, z_m , using eq. 5, as:

170

171 8. $z_m = z_b + a_s \cdot \chi_{u,k}(m, n, U^*, K^*) = g(a_s, m, n, U^*, K^*)$

172

173 We estimate the robustness of our direct model, expressed through the function g , by computing
174 the difference between modeled elevation, z_m , and measured elevation, z , using the cost
175 function, ϕ , using the L2 norm:

176

177
$$9. \phi(m, n, a_s, U^*, K^*) = ||g(a_s, m, n, U^*, K^*) - z||_2$$

178

179 Where z is the elevation data, typically obtained from a digital elevation model (DEM).

180

181 3.1.2 Parameterizing uplift patterns using B-spline functions

182

183 We parameterize the spatial variability of uplift, $U^*(\vec{x})$, using B-spline functions (De Boor,
184 1978; Piegl & Tiller, 1997). Constructed from a series of piecewise polynomial basis functions and
185 defined between a grid of control points known as knots, B-splines serve as interpolating
186 functions where a coefficient, Q , at each knot controls the shape of the uplift pattern (See Text
187 S1). This approach provides the flexibility to modify uplift patterns by simply adjusting Q values
188 without being restricted to a predetermined functional form, thus ensuring a smooth and
189 continuous representation of spatial variability in rock uplift.

190

191 3.1.3 Parameterizing spatial Erodibility

192

193 Spatial variations in erodibility are typically driven by changes in lithology (Campforts et
194 al., 2020; Ellis & Barnes, 2015; B. Gailleton et al., 2021; Harel et al., 2016) and the occurrence of
195 major faults, which inherently display areal discontinuities. Thus, using continuous mathematical
196 functions, such as B-splines, polynomials, or Gaussians, to represent variations in erodibility
197 would misrepresent the inherently piece-wise nature of this field. We instead delineate
198 lithological units (e.g., from geological maps) and invert for their piece-wise uniform erodibility
199 k_i across various lithological domains (numbered by i)

200

201 3.1.4 Parameterizing climatic modulation of erosion

202
203 We incorporate climatic variations by weighting the drainage area with precipitation rates
204 and computing an effective volumetric discharge, $A_Q(x)$. This method is commonly employed in
205 fluvial topographic analysis to assess the impacts of variable precipitations, both spatially and
206 temporally (Babault et al., 2018; Leonard et al., 2023; Leonard & Whipple, 2021). The adjusted
207 discharge, $A_Q(x)$, at point x is defined by integrating the drainage area, A, weighted by the
208 precipitation rate, P, from the river source, x_s , downstream to the base:

209
210
$$10. A_Q(x) = \int_{x_b}^{x_s} P(x)A(x)dx$$

211
212
213 3.2 Inversion scheme

214
215 To identify plausible combinations of a_s, m, n, U^* and K^* , we minimize the misfit
216 between the modeled and measured elevation (eq. 9) using a Bayesian quasi-Newton scheme
217 (Tarantola, 2005) in an iterative fashion:

218
219
$$11. t_{l+1} = t_l + \mu(G^t C_D^{-1} G + C_M^{-1})^{-1}(G^t C_D^{-1}(z_m - z_{obs}) + C_M^{-1}(t_l - t_0))$$

220
221 Where t_l is a vector comprising all model parameters at iteration l . G is the Jacobian
222 matrix determined using centered finite difference such that:

223
224
$$12. G_i = \frac{\partial \phi}{\partial m}$$

225 z_{obs} is a vector of observations consisting of measured elevation z , z_m is the modeled elevation
226 of rivers computed using $g(t_l)$, C_M is the a priori covariance matrix, C_D is the observation
227 covariance matrix, i is an index delineating model parameter and μ is a constant between 0 and
228 1. We employ an initial guess, t_o , assuming $m=0.5$, $n=1$, $a_s = 0.1$ as well as B-spline and
229 erodibility coefficients that describe uniform uplift and erodibility patterns.

230 We configure the covariance matrix C_m with diagonal terms equal to 0.01 (standard
231 deviation of 0.1) for the entries corresponding to m , n , and a_s , and 1 for B-spline weights and
232 dimensionless erodibility coefficients, reflecting a lack of a priori knowledge about spatial
233 variability in the uplift and erodibility patterns. We consider a solution m_l satisfactory when
234 $\frac{\phi(m_{l+1}) - \phi(m_l)}{\phi(m_o)} < 0.01$.

235 Upon reaching an optimal solution, we can use the recovered B-spline parameters to
236 characterize the uplift pattern along the rivers used in the inversion as well as across the entire
237 rectangular domain bounded by the river network (Text S1). The geometry of the river network
238 may leave some knots poorly constrained due to the absence of nearby rivers. To address this,
239 we compute uplift only within catchments feeding the rivers used in our analysis, ensuring that
240 the involved knots have non-negligible values based on the sensitivity parameter, $\text{diag}(G^T \cdot G)$.
241

242 4 Application to synthetic landscapes

243

244 We assess the reliability of our methodology, which inherently assumes steady-state
245 incision of channels, across a range of synthetic landscapes. These artificial terrains exhibit
246 varying degrees of deviation from the stream power law and include hillslope diffusion, sediment
247 deposition, orographic effects, spatial changes in erodibility, and temporal shifts in uplift rates
248 (e.g., Leonard & Whipple, 2021; Merritt et al., 2003; Roering et al., 1999, 2001; Whipple, 2009).
249

250 4.1 Generating synthetic landscapes

251

252 We model synthetic terrains, incorporating both fluvial and hillslope erosion along with
253 deposition dynamics based on the CIDRE model framework defined by (Carretier et al., 2016) :

254

255
$$13. \frac{dz}{dt} = \dot{d}_f - \dot{e}_f + \dot{d}_h - \dot{e}_h + U(x, y)$$

256

257 where \dot{d}_f is the fluvial deposition rate, \dot{e}_f the fluvial incision rate, \dot{d}_h the hillslope diffusion flux,
258 \dot{e}_h the hillslope erosion rates and $U(\vec{x})$ is the imposed tectonic uplift. The fluvial component relies
259 on a formulation originally developed by Davy & Lague (2009) where erosion and sediment
260 entrainment are functions of stream power and sediment length deposition. The hillslope laws
261 are a hybrid between linear and non-linear landscape diffusion models, reproducing both end-
262 members (see Carretier et al., 2016 for full details).

263 We use an explicit finite difference numerical scheme to solve equation (13) where spatial
264 discretization is done along a 100 X 100 km regular 2D grid with 400 m spacing in the x and y
265 directions. We use different graph theory algorithms to organize our nodes into an upstream to
266 downstream topological order (see Gailleton et al., 2024 for details on the numerical structure)
267 and use the carving algorithm of (ordonnier et al., (2019) to resolve local minima. We employ a
268 time step of 500 years and run synthetic models over 5 million years to ensure the landscape
269 reaches a topographic steady state, resulting in negligible elevation variations over time. Lastly,
270 we use $n = 1$, $m = 0.45$ and rock erodibility, k , of $2 \cdot 10^{-5} m^{(0.9)} \cdot yr^{-1}$. We parameterize the
271 imposed tectonic uplift field using an asymmetrical 2D Gaussian- function:

272

273
$$14. U(x, y) = u_0 \cdot \exp [-a(x - x_0) + 2b(x - x_o)(y - y_0) + c(y - y_0)^2]$$

274

275 Where $a = \frac{\cos^2(\theta)}{2\sigma_x^2} + \frac{\sin^2(\theta)}{2\sigma_y^2}$, $b = -\frac{\sin(2\theta)}{4\sigma_x^2} + \frac{\sin(2\theta)}{4\sigma_y^2}$, $c = \frac{\sin^2(\theta)}{2\sigma_x^2} + \frac{\cos^2(\theta)}{2\sigma_y^2}$, θ is the azimuth of the
276 long-axis of the Gaussian, x_o , σ_x and y_0 , σ_y are the center and width of the gaussian along the x
277 and y directions, respectively. Lastly, we assume a characteristic uplift rate, u_0 , of $1.2 mm \cdot$
278 yr^{-1} (Fig. 1).

279

280 4.2 Inversion of synthetic landscapes

281 We apply our inversion scheme on simulated synthetic landscapes and select the 8000
282 most downstream nodes from the largest catchments to guarantee our inversion outputs are not
283 secondarily influenced by the number of observations (z_{obs}). To mimic the uncertainty in real
284 elevation data we add noise using randomly sampled values from a normal distribution centered

285 around 0 with standard deviation, ε , of 10 m. We then invert the resulting landscapes using two
286 different schemes. The first solves for 84 parameters including m, n, a_s and the control points for
287 spatially-varying uplift with a 2D cubic B-spline function along 6 knots in the y and x direction.
288 The second assumes a uniform uplift pattern and fits landscape constants m, n and a_s only (eq.
289 6). We estimate how well the inversions perform by comparing recovered uplift and elevation
290 with synthetic modeled elevation and imposed uplift using the root mean square (RMS) metric:
291

$$15. RMS = \sqrt{\frac{1}{N} \sum_{i=0}^N (q_i^r - q_i^m)^2}$$

292 Where q_i^r is recovered value i , q_i^m imposed value i and N total number of measurements
293 in the dataset.

295

296 4.3 Results

297 4.3.1 Detachment-limited scenario

298 We produce a synthetic landscape subject to an ellipsoidal uplift function (Table S1; Fig. S1)
299 where erosion is exclusively detachment-limited (Fig. 1A). Once in steady state, we measure the
300 landscape's drainage area, flow direction, and the distance between river nodes required for
301 computing χ . We then use these landscape properties and apply two inversion mechanism: (1)
302 solving for uplift pattern, and (2) assuming uniform uplift.

303 Our first inversion performs well, retrieving outputs that are almost identical to those imposed.
304 The RMS value for uplift is 0.01, indicating that the inverted uplift for the 8,000 river nodes used
305 closely matches the imposed tectonic uplift (Fig. 1). Additionally, our inverted elevation closely
306 mirrors the measured elevation, with discrepancies reflecting the introduced noise, ε , leading to
307 an RMS value of 10 meters. This accuracy is illustrated nicely by the linear shape of the final river
308 elevation profiles in χ -space, a_s , where the scatter reflects the noise (Fig. 1C). In contrast, the
309 inversion assuming uniform uplift returns RMS values that are 7 times higher and fails to
310 accurately determine landscape constant m, n and a_s (Fig. 1C).

311 Once we have established that our inversion can accurately recover landscape properties
312 in this idealized case, we proceed to test its limitations by challenging the assumptions it relies
313 on.

314

315 4.3.2 Scenarios deviating from the Detachment-limited endmember

316 *4.3.2.1 Sediment transport length*

317 We apply our inversion scheme to synthetic landscapes featuring varying degrees of
318 sediment deposition, hillslope diffusion, orographic effects, spatial variations in erodibility, and
319 temporal changes in uplift rates. For the sediment deposition case, we generated 20 identical
320 landscapes, differing only in the value of the characteristic sediment transport length (e.g.,
321 Carretier et al., 2016; Merritt et al., 2003). For transport lengths longer than 1 km, our inversion
322 accurately recovers landscape parameters with RMS elevation and uplift values comparable to
323 the noise we added, ε (Fig 2A1 & 2B1). Landscapes characterized by transport length shorter than
324 1 km generate greater relief owing to the additional sediment deposition. Consequently,
325 inverting these models yields less accurate inversion results, with RMS values 5 to 30 times higher
326 for both elevation and uplift (Fig 2A1 & 2B1). Interestingly, even as the landscape deviates
327 significantly from the detachment-limited case, the inversion aims to maintain the imposed $\frac{m}{n}$
328 ratio, capturing this "detachment-limited property" of the landscape (Fig. S2).

329 *4.3.2.2 Diffusion*

330 To test the effect of hillslope diffusion on our inversion, we modeled and inverted 50
331 landscapes, each employing a distinct diffusion parameters k_d controlling topographic dispersion
332 across the landscapes (Carretier et al., 2016). For k_d smaller than $10^{-2} \text{ m} \cdot \text{yr}^{-1}$ the inversion
333 outputs almost perfectly retrieved the parameters of the landscape (Fig 2A2 & 2B2). For higher
334 diffusion values of $10^{-2} - 10^{-1} \text{ m} \cdot \text{yr}^{-1}$, the retrieved uplift function exhibits pronounced
335 uncertainties but can still capture the original signal (Fig. S3). For $k_d > 10^{-2} \text{ m} \cdot \text{yr}^{-1}$, the river
336 network ceases to represent a typical mountain range drainage system (Fig. 2B2). This is reflected
337 in the poor performance of the inversion showing RMS values 10-30 times higher than the best
338 retrieval values, partly due to the lack of river nodes in the center of domain(Fig. 2A2).

339 4.3.2.3 *Precipitation*

340 Spatial variability in climatic conditions can also significantly influence landscapes (e.g.,
341 Molnar & England, 1990), particularly in mountain ranges with orographic precipitation on the
342 windward flanks and drier conditions on the leeward sides (e.g., Bookhagen & Burbank, 2010).
343 To incorporate this effect into the evaluation of our synthetic models , we index precipitation on
344 elevation using the equation $p(z) = \alpha_o e^{-\frac{z}{h_0}}$, where α_o is precipitation at sea level, Z elevation,
345 and h_0 a reference elevation (Hergarten & Robl, 2022). To reflect reduced rainfall along the lee
346 side of the landscape we reduce the α_o value there, effectively generating uneven precipitation
347 $p(x, z)$ (e.g., Figs. 2B3, S3D1 and S3D2). We then simulate 50 landscapes using the effective
348 volumetric discharge A_Q (eq. 10), modulated by precipitation $p(x, z)$ with each terrain
349 characterized by a distinct h_0 .

350 Our inversion assuming that water discharge simply scales with only drainage area (A)
351 accurately recovers landscape parameters for $h_0 < 0.5 \text{ km}$. For h_0 values above 0.5 km, retrieval
352 inaccuracies increase, worsening with larger values (Figs 2A3 & 2B3). However, when we use A_Q
353 (eq. 10) in our inversion, it accurately retrieves the correct landscape parameters, effectively
354 determining elevation, uplift (Fig 2A3), and m , n and a_s (Fig. S3). Our inversion's ability to
355 accurately retrieve landscape parameters is particularly noteworthy given that A_Q undergoes
356 significant changes as the landscape evolves with time and we use the values from the final
357 timestep.

358 4.3.2.4 *Lithology*

359 Lithology is an additional spatially variable parameter influencing landscape evolution.
360 We explore its significance by modeling 50 landscapes each featuring a 20 km wide zone with low
361 erodibility, k_s , varying by up to an order of magnitude from the background erodibility, k_w , $2 \cdot$
362 $10^{-5} m^{(0.9)} \cdot yr^{-1}$. The sharp change in erodibility results in landscapes with two distinct
363 topographic highs: one aligned with the imposed uplift pattern and another associated with the
364 low erodibility zone where the ratio of altitudes between these peaks is linked to $\frac{k_w}{k_s}$ (e.g., Fig.
365 2B4, S5D1 and S5D2).

366 For $\frac{k_w}{k_s} > 0.5$ our standard inversion performs well, almost unaffected by the addition of
367 a stronger rock section (Fig. 2A4). However, for $\frac{k_w}{k_s} < 0.5$, the standard inversion scheme
368 struggles to accurately capture the current properties of the landscape, and the retrieved uplift
369 values reflect the region of lower erodible domain rather than the imposed uplift shape (Fig.
370 2A4). However, when we invert for erodibility (see section 3.1.3) as well as U^* , m , n and a_s the
371 inversion scheme excels in accounting for elevation and uplift pattern (Figs. 2A4 and S5). The
372 recovered and imposed erodibility ratio are in remarkably good agreement (Fig 2A4) suggesting
373 that our inversion scheme is capable of accounting for spatial changes in rock erodibility.

374 *4.3.2.5 Rock uplift rate*

375 To investigate the impact of time-varying tectonic forcing, we bring a detachment-limited
376 landscape to a steady state and then instantaneously increase the uplift rate by a factor of three,
377 similar to observed changes in uplift history along normal fault systems (e.g., Goren et al., 2014;
378 Smith et al., 2024). We proceed to simulate the landscape for an additional 1.6 million years until
379 it reaches a new equilibrium (calculated using Equation (3) ;Fig. S6) and invert landscapes
380 snapshots retained at intervals of 0.1 million years.,

381 Our inversion responds to the step change in uplift rate with a minor increase in RMS
382 values for the retrieved elevation. Conversely, the inversion shows greater deviations in the
383 recovered uplift pattern and in the m , n and a_s values than in elevation (Figs. 2A5, 2B5 & S7). This
384 is because the inversion effectively compensates with adjustments in other parameters to return
385 accurate elevation values. This illustrates the challenge of determining whether a natural
386 landscape is in steady state based solely on elevation errors. After about half the time needed to
387 reach equilibrium, the inversion returns values that align well with the imposed parameters (Fig.
388 2A5). This stabilization in parameter retrieval is clearly illustrated by a_s values (incorporating the
389 updated u_0 value) which reach their new steady-state levels approximately 0.8 million years after
390 the step change. We attribute the inversion's ability to retrieve the imposed values before the
391 entire landscape reaches steady state to the fact that a significant portion of the landscape is
392 already in equilibrium, with only the upstream sections of rivers still in transition. This is
393 evidenced by the large misfit values at the river tips, which, unlike in steady-state conditions, are
394 more evenly distributed across the landscape (Fig. S8). We note that we observe a similar pattern

395 in landscapes subjected to temporal changes in uplift pattern over a given time period (Text S2
396 & Fig. S8).

397

398 5 Application to natural landscapes

399 5.1 Selection of sites

400

401 To test the real-world applicability of our inversion scheme, we apply it to both divergent and
402 convergent tectonic settings. For the divergent setting, we analyze five landscapes shaped by
403 normal faults, where our understanding of the crust's flexural response to faulting provides a
404 reliable test bed for comparing our inverted uplift patterns. For the convergent setting, we focus
405 on a well-studied, approximately 200 km-wide section of the Himalayas and compare our results
406 to previous uplift estimates derived from geomorphological markers.

407

408 5.1.1 Landscapes shaped by normal faults

409

410 We apply our inversion methodology to natural landscapes shaped by half-graben border
411 faults where kilometer-scale offset along the fault flexes the brittle upper crust, yielding a 1-D
412 rock uplift field that decreases with across-strike distance from the fault (Fig S10; Weissel &
413 Karner, 1989). Thicker and stronger faulted layers typically produce longer uplift decay lengths,
414 extending further into the footwall. This relatively simple pattern makes it an appealing
415 benchmark case, and has been leveraged in previous geomorphological tectonic studies (e.g.,
416 Goren et al., 2014; Ellis & Barnes 2015). Recovering systematic trends in the uplift shape
417 consistent with flexural properties of several landscape would provide additional constraints on
418 the validity of our inversion.

419 To this end, we study five landscapes with varying faulted layer thicknesses (Table S2; Olive
420 et al., 2022): The Paeroa Range (Paeroa fault ,New Zealand), Sandia Mountains (New Mexico,
421 USA), Wassuk Range (Nevada, USA), Lehmi Range (Lehmi Fault, Idaho, USA), and Kipengere Range
422 (Livingstone Fault, Lake Malawi, Tanzania). We analyze river sections located far from fault tips

423 (Densmore 2007; Ellis & Barnes, 2015), ensuring that uplift is predominantly a function of distance
424 from the fault, allowing us to use the faster 1D inversion. However, to demonstrate the
425 applicability of our 2-D inversion scheme, we apply it to the Lemhi range where we specifically
426 focus on the southern section near the fault tip because its uplift pattern is well-documented and
427 has been shown to diminish southward (Fig. S10; Densmore et al., 2007).

428 We include erodibility variations for the Sandia mountains, as they feature two clear and
429 distinct lithological domains comprising predominantly limestone on the Eastern side and granite
430 on the Western side (Williams & Cole, 2007), which typically show different erosional properties
431 (Fig 3C2). We assume uniform erodibility in other studied landscapes as these exhibits relatively
432 uniform lithology. Lastly, we note that we did not account for spatial changes in precipitation
433 here. The Kipengere Range showed little evidence of a correlation between precipitation and
434 altitude in documented rainfall trends in the past 23 years (Fig S11; Global Precipitation
435 Measurement; GPM; Huffman et al., 2015) despite its 1.5 km relief and an expected strong
436 orographic effect. This suggests that orographic effects are even less important in the other
437 gentler landscapes.

438

439 5.1.2 The Himalayas

440

441 We apply our inversion scheme to a well-studied, approximately 200 km-wide section of
442 the Himalayas, where previous studies have identified high uplift rates occurring around 100 km
443 from the main Himalayan thrust, with slower uplift rates observed farther away (Dal Zilio et al.,
444 2021; Godard et al., 2014; Lavé & Avouac, 2001). We exclude the Siwalik Hills from our analysis
445 as rivers in this region are not predominantly detachment-limited. Additionally, we omit
446 catchments north of the Himalayan water divide extending to the Tibetan Plateau, as these
447 require separate, higher base levels, which would limit the spatial extent of our analysis.

448 Our inversion accounts for four distinct erodibility sections, delineated by the main
449 lithological units in the area (Fig 4C; Carosi et al., 2018). To incorporate the pronounced climatic
450 patterns in the Himalayas (e.g., Bookhagen & Burbank, 2010), we compute A_Q using eq (10),

451 based on the average spatial distribution of the past 23 years of satellite-based precipitation data
452 (Fig. 4D; Huffman et al., 2015).

453

454 [5.2 Inversion of natural landscapes](#)

455

456 We use 30 m-DEM of landscapes obtained by the Shuttle Radar Topography Mission (Farr
457 et al., 2007) . We extract nodes (pixels) corresponding to major rivers (Figs. 3B1-3B5 and 4A),
458 defined as those draining areas larger than a set threshold and above a set base level elevation
459 (Table S2). These thresholds are carefully selected to balance computational efficiency for the
460 inversion calculations with an accurate representation of the landscape's fluvial sections. For
461 landscapes shaped by normal faults, our aim is to include river nodes that cover the entire decay
462 length of the fault-induced uplift. However, this is often complicated by river nodes near the
463 fault, which are typically located on hanging wall-facing cliffs that drain small areas or lie
464 underwater. Consequently, we calculate the rivers' distance from the outlet, drainage area, and
465 elevation (O'Callaghan & Mark, 1984), and rotate their geographical coordinates to align with an
466 along-fault strike and across-fault strike coordinate system. We estimate their connectivity and
467 flow path using the steepest descent algorithm (O'Callaghan & Mark, 1984).

468 We compute multiple inversion scenarios for each landscape, varying the number of B-
469 spline nodes, ensuring the distance between B-spline nodes is at least 5km (Text S1). We report
470 the inversion that minimizes the Akaike Information Criterion (AIC) (Akaike, 1974; Bishop, 2006).
471 The AIC includes a penalty term to prevent potential overfitting caused by the addition of
472 superfluous parameters to the model (Text S3). We also assume an elevation uncertainty of 30
473 meters, a value that has been deliberately increased from the reported SRTM dataset
474 uncertainty. This additive inflation addresses our model's limitations in capturing detailed terrain
475 features, as highlighted in the synthetic inversion cases. Employing such an approach is common
476 practice across various parameterizations in physical modeling, aiming to better represent the
477 inherent uncertainties without exhausting every detail (e.g., Anderson, 2007). Lastly, we note
478 that for the Malawi landscape case, we set the covariance matrix to values of 10^{-4} (standard

479 deviation of 10^{-2}) for m and n . This adjustment was necessary to avoid inverted m and n values
480 that produced unrealistically long knickpoint travel times (eq. 3).

481

482 5.3 Results

483 5.3.1 Landscapes shaped by normal faults

484

485 Our 1D inversions consistently reveal an uplift pattern that decreases with greater
486 distances from the fault along the footwall (Fig. 3A-D). The recorded wavelength correlates with
487 the thickness of the brittle faulted layer constrained by the maximum depth of recorded
488 earthquakes (Olive et al., 2022; Table S2; Figs. 3A1-A4) where the Paeroa Range (Fig. 3A1) exhibits
489 the narrowest uplift wavelength followed by the Sandia (Fig. 3A2), Wassuk (Fig. 3A3), and
490 Kipengere (Fig. 3A4) ranges.

491 For the Sandia Mountains, inversions assuming both uniform and variable erodibility yield
492 nearly identical uplift wavelengths. However, the first yields an unrealistic peak in the uplift field
493 at a distance of 8 km from the fault which we attribute to variations in erodibility (Fig. 3A2). An
494 inversion that accounts for a different erodibility in the Western and Eastern sides of the range
495 indeed yields a more straightforward uplift field that continuously decays with distance to the
496 fault. It also produces less scatter in χ values (Fig. 3B2) and determines that Sandia granite (West
497 side) is 2.2 times more erodible than the Madera formation limestone (East side, Fig. 3C2). The
498 latter is consistent with the notion that high infiltration rates over carbonate landscapes deprive
499 rivers from water and therefore erosive power, while much greater surface runoff enhances
500 granite denudation. This results underscores the importance of considering variable erodibility
501 when inferring tectonic uplift fields.

502 We highlight that our inversion method is designed to recover the coefficients controlling the B-
503 spline knots (see Figs. S12-S15 for the posterior distributions of all inverted parameters) , which
504 can be used to describe uplift not only along the rivers utilized in the inversion but also across all
505 catchments feeding those rivers (see section 3.5.1). While this capability is clearly demonstrated
506 in the 1D inversion cases (Figs. 3C1-4), its true strength lies in capturing complex spatial attributes
507 across two dimensions. For example, our 2-D inversion for the Lemhi landscape effectively

508 captures the spatial variations in uplift expected near the tip of a normal fault within the Lemhi
509 Range. It shows diminishing uplift within 10 km to the fault tip (Fig. 3A5), aligning with previously
510 documented k_{sn} values in the region (Densmore et al., 2007), and a general decrease in uplift
511 with increasing distance from the fault axis (Fig. 3C5). These observations demonstrate our
512 model's ability to accurately infer two-dimensional variations in uplift.

513 Similar to our synthetic landscapes (Figs. 1C, S2-5), inverting for uplift patterns yields RMS
514 values that are 2-3 times better than those assuming a uniform uplift pattern (Fig. 9). This is
515 visually supported by the tight alignment of χ values around the recovered a_s particularly in the
516 Wassuk range case where χ values that do not account for uplift gradients form three distinct
517 branches in contrast to the neatly aligned χ values for the inversion that accounts for uplift
518 variations (Fig. 3B3). Additionally, the average recovered m/n ratio is closer to $\theta = 0.45$, a value
519 considered typical for natural landscapes (Boris Gailleton et al., 2021; Mudd et al., 2014; Snyder
520 et al., 2000). The Wassuk Range shows relatively large deviation with an m/n ratio of 0.22.
521 However, when we invert the landscape while fixing $n=1$ and $m=0.45$ we recover an uplift pattern
522 that closely resembles the original with an RMS value larger by 1.4 (Fig. S16).

523 We note that the Malawi landscape exhibits the highest RMS value compared to other
524 landscapes shaped by normal faults (Fig. 3). The steep, incised topography of the Kipengere Ridge
525 indicates strong fluvial incision driven by detachment-limited processes near the fault. However,
526 fluvial incision driven by the Livingstone fault system extend into smoother, sediment-filled
527 valleys about 40 km away, where hillslope diffusion and sediment deposition contribute to
528 elevation misfits. These contrasting landscape features likely explain the larger misfits in Malawi
529 compared to other landscapes with smaller RMS values.

530

531 5.3.2 The Himalayas

532

533 Our inversion results for the Himalayan section reveal a distinct region of uplift
534 approximately 100 km N-NE of the main frontal thrust, extending from the eastern to the western
535 end of the study area (Fig. 4A). This finding aligns well with previous estimates (Fig. 4G) derived
536 from fluvial incision rates observed in terraces, channel geometry (Lavé & Avouac, 2001), ^{10}Be

537 concentrations in detrital sediments (Godard et al., 2014), and 1-D river profile analysis (Meade,
538 2010). Additionally, we identify a second uplift peak closer to the frontal thrust on the
539 southwestern end. The uncertainty associated with this peak is larger (Fig. 4C) due to the sparse
540 river network in the region, which limits the constraints on the B-spline coefficients and reduces
541 our confidence in interpreting this feature.

542 In contrast to the Sandia Mountains (Fig. 3A2), where erodibility values exhibited
543 significant contrast and strongly influenced the inverted uplift patterns, the recovered erodibility
544 values in the Himalayas (e.g., Fig. 4D) are relatively uniform, with values within one standard
545 deviation of each other (Table S3). This suggests that spatial variations in erodibility does not play
546 a major role in shaping the landscape in this section of the Himalayas.

547 To assess the influence of climate patterns, we performed an additional inversion that
548 excluded the effects of variable precipitation. Although this inversion resulted in RMS values that
549 were higher by a factor of 1.3 (Fig. 4B), it still revealed similar overall features, including an uplift
550 peak extending from east to west (Fig. 4F). Interestingly, when precipitation variability was
551 excluded, the highest uplift region shifted from the western side to the central area of the
552 domain. This shift illustrates how increased rock uplift is required to offset larger drainage areas
553 in the west when accounting for variable precipitation (Fig. 4A).

554

555 6 Discussion

556 6.1 Applicability and limits of the methods: Insights from Synthetic landscapes

557

558 By examining synthetic landscapes we show that pronounced hillslope diffusion and
559 sediment transport lead to reduced accuracy of recovered landscape properties. Significant
560 sedimentation in mountain ranges depart from the detachment-limited models we use, leading
561 to discrepancy between inverted and imposed uplift (Fig. 2B1). Satellite imagery offers a reliable
562 method to identify regions with pronounced sediment cover, allowing us to focus on basins with
563 predominantly bedrock rivers (e.g., Perron & Royden, 2013; Wobus et al., 2006).

564 The impact of hillslope diffusion is more uniform across the landscape and thus more
565 challenging to circumvent. However, our synthetic landscape analyses suggest that only in case
566 of exceptionally pronounced hillslope diffusion do our recovered uplift patterns starkly diverge
567 from the imposed uplift (see Litwin et al., in rev. for a corrective solution). Such high values of
568 hillslope diffusion should form natural landscapes with smooth features that are easy to identify
569 and avoid (e.g, Fig. 2B2). We note that our synthetic hillslope diffusion model does not account
570 for changes in diffusion rates across landscapes (e.g., Auzet & Ambroise, 1996; Bontemps et al.,
571 2020; Matsuoka, 1998). Additionally, our underlying assumption is that channel width is a power-
572 law function of discharge manifested as a change in the effective exponent m. In reality, however,
573 river channels width may vary locally, with narrower channels increasing erosion (Lavé & Avouac,
574 2001; Yanites et al., 2010) ,which in our case would likely result in unrealistic high inverted uplift
575 pattern.

576 Our study of synthetic landscapes adjusting to a change in uplift rates and patterns reveals
577 that if more than half the required time to reach a new equilibrium has passed, our inversion
578 accurately recovers the uplift signal (Fig. 2A5). In our simulations, temporal changes are modeled
579 as instantaneous steps while in natural settings, these variations may unfold over extended
580 periods. For example, Smith et al. (2024) used river profiles along the normal fault-bound
581 Wasatch Range, demonstrating that uplift rates fluctuate temporally up to threefold within as
582 little as 400 ky suggesting that the landscape may never achieve quasi steady state. Similarly,
583 when we model changes in uplift rates over comparable durations, our inversion method
584 successfully recovers uplift patterns closely resembling the imposed ones (Text S3; Fig S17),
585 despite the landscapes being far from steady state. This echoes our findings from instantaneous
586 step changes experiment (Fig. 2A5), confirming that even when landscapes are not in steady
587 state, our inversion can retrieve uplift patterns that mirror the imposed ones. This indicates that
588 when we apply our inversion to natural landscapes, we likely extract a value of a_s that reflects a
589 time-averaged window and an uplift pattern that shows minor deviation from the time-averaged
590 tectonic uplift. This is partly because working in the χ framework lets us treat the river network
591 as a cohesive system, integrating the contributions of all river nodes, as opposed to local
592 approaches such as k_{sn} .

593 In contrast, temporal variations in spatial uplift pattern are typically slower and less
594 frequent. Adjustments in fault orientation or dip angle, which can alter uplift patterns, are either
595 slow and progressive (e.g.,Olive & Behn, 2014; Oryan & Buck, 2020) or result in the formation of
596 new faults rather than modifying existing ones (e.g., Taylor & Switzer, 2001). These new faults
597 are likely to form far from the original faults and may not significantly impact the associated uplift
598 pattern. Our synthetic landscape experiments exploring the effects of gradual temporal changes
599 in uplift patterns demonstrate that, as long as the imposed changes are slow enough, our method
600 accurately extracts uplift patterns that closely resemble the original ones (Text S4; Fig S18).

601 Our synthetic landscape analyses also demonstrate that spatial variations in erodibility and
602 precipitation can significantly alter the recovered uplift pattern with discrepancy amounting to
603 RMS values of 10-5 times the original signal (Fig. 2A4). Nevertheless, we demonstrated that the
604 inversion is capable of accounting for those. This is crucial as current methods to extract uplift
605 patterns from landscapes often rely on k_{sn} (e.g., Castillo et al., 2014; Densmore et al., 2007;
606 Ponza et al., 2010; Su et al., 2017) which cannot directly distinguish between erodibility and uplift
607 given spatial varying erodibility. Our method offers a way to discern the two provided that we
608 can predefined regions with different erodibility levels based on lithological maps.

609

610 6.2 Performance on natural landscapes

611

612 Our analysis of natural landscapes highlights the effectiveness of our inversion method. For
613 landscapes shaped by normal faults, we demonstrate that the decay length of the uplift field
614 away from the fault is directly linked to the thickness of the brittle upper crust (Figs. 3A1-4),
615 consistent with standard models of normal fault-induced flexure, where a thicker elastic layer
616 typically produces a broader uplift profile (e.g., Goren et al., 2014; Nadai, 1963; Weisssel & Karner,
617 1989) We demonstrate that our method can robustly extract this signal, even when it is intricately
618 linked with spatial variations in erodibility (Figs. 3A2). Additionally, we retrieve smaller uplift rates
619 around the Lemhi fault tip (Fig. 3A5), aligning with previous uplift estimates (Densmore et al.,
620 2007) and the notion that slip vanishes over a short distance near fault tips (Ellis & Barnes, 2015;
621 Roberts & Michetti, 2004). Our analysis of the Himalayan landscape (Fig. 4) further validates the

622 effectiveness of our method in retrieving realistic uplift patterns while accounting for climatic
623 variations, showing strong alignment with previous estimates based on geomorphological
624 markers (Fig 4G). This consistency across different tectonic settings underscores the robustness
625 of our inversion approach in accurately recovering uplift patterns from natural landscapes.

626 This said, pinpointing which aspects of the retrieved signal are linked to temporal changes
627 presents an intriguing challenge. Our analysis of synthetic landscape shows we can recover uplift
628 pattern similar to the imposed one, even when introducing a fivefold fluctuation in the uplift rate
629 through time (Text S3; Figs. S17). The uplift field driven by tectonics should only change steadily
630 (e.g., as the fault rotates to different dips, or lengthens along strike), as we expect major
631 disruptions in uplift to be due to the initiation of new faults / abandonment of old ones (see
632 section 5.1).

633 This leads us to focus on determining whether the signal associated with slip on a currently
634 active fault ongoing fault slip has reached equilibrium. The time required for a knickpoint to travel
635 upstream from the base level, calculated using eq. (3) and our recovered parameters a_s , m, n,
636 along with estimates of uplift rate u_0 and erodibility value k_0 , suggests that all but one of the
637 normal fault-bound landscapes have reached equilibrium since fault initiation (see Text S5; Fig
638 S19; Table S2). The Malawi landscape exhibits a travel time of approximately 35 million years,
639 extending well beyond the initiation time of the Livingstone Fault, estimated at ~23 million years
640 (Mortimer et al., 2016). Even if we consider the time to reach steady state is cut by half as
641 indicated by our analysis of synthetic landscapes, it is likely that regions far from the fault have
642 not reached a steady state. This could explain the transition to a more gradual incline in the
643 recovered uplift pattern observed approximately 10 km from the fault (Fig. 3D).

644 In the Himalayas, we are fortunate to have an abundance of geomorphological markers
645 that measure uplift and denudation rates across various timescales, allowing us to qualitatively
646 assess whether the landscape is in a quasi-steady state. These markers include rock-uplift rate
647 estimates from river-profile analyses (Lavé & Avouac, 2001), ^{10}Be concentrations in fluvial
648 sediments (Godard et al., 2014), apatite fission-track cooling ages (Robert et al., 2009) and
649 thermochronological data (Herman et al., 2010), capturing processes operating over time scales
650 ranging from thousands to millions of years. All these geomorphological markers indicate a peak

651 in uplift rate at approximately 100 km from the main frontal thrust (Fig. 4G). This consistency in
652 spatial patterns across different temporal scales highlights the temporal persistence of tectonic
653 signals and suggests that the Himalayan landscape may approach a steady state.

654 Additional support for the success of our inversion lies in its ability to extract θ values that
655 closely aligned with the expected value of ~ 0.45 (Figs. 3 & 4). This suggests that our method
656 remains effective even in the absence of strong constrains on the reference concavity index ($\frac{m}{n}$),
657 a parameter challenging to constrain (Gailleton et al., 2021; Mudd et al., 2014, 2018; Snyder et
658 al., 2000). Nonetheless, we note that our initial choice of m and n values may lead to convergence
659 at a local minimum (Tarantola, 2005) which may prevent exploring minima associated with
660 similar concavity values with different m and n values. Using alternative approaches such as the
661 Metropolis-Hastings Markov Chain Monte Carlo (MCMC), would minimize the likelihood of
662 converging to a local minima by thoroughly sampling the posterior probability density function
663 and providing a comprehensive exploration of the parameter space. (e.g., Dal Zilio et al., 2020;
664 Gardonio et al., 2018; Jolivet et al., 2020). However, MCMC is computationally expensive,
665 requiring millions of forward model evaluations, making it impractical for the more than 2500
666 separate inversions conducted in this study. Inverting large-scale landscapes, on the other hand,
667 would necessitate significantly more B-spline nodes and inverted parameters, diminishing the
668 benefits of the quasi-Newton scheme and making MCMC a more appropriate candidate for the
669 choice of inversion scheme.

670 Finally, our analysis of natural landscapes provides an opportunity to examine the
671 theoretical predictions of lithospheric flexure (Nadai, 1963; Weissel & Karner, 1989). The
672 deformation associated with kilometer long offset accommodated along normal faults is typically
673 approximated as a thin, broken elastic plate of thickness, T_e , flex above a viscous half-space. This
674 predicts that uplift due to flexure diminishes exponentially with greater distance from the fault,

675 as $e^{-\frac{x}{\alpha_b}}$, and that uplift wavelength, α_b , is linearly proportional to $T_e^{\frac{3}{4}}$ by a coefficient that reflects
676 the elastic properties of the lithosphere (Text S6; Nadai, 1963). Adopting typical properties of the
677 lithosphere suggests a relationship of $\alpha_b = 45 \cdot T_e^{\frac{3}{4}}$, however, our derived uplift profiles, in
678 conjunction with the elastic plate thickness, suggest a correlation characterized by a coefficient

679 of 1.5, significantly lower than the expected value of 45 (Text S6; Fig. S20-21). This discrepancy
680 has also been observed for the Basin and Range's Inyo mountains (Goren et al., 2014) and likely
681 arises from the theory's neglection of inelastic flexure and isostatic adjustment associated with
682 erosion and the transportation of sediment to the hanging wall basins. Advanced numerical
683 simulations that incorporate surface processes and the dynamic behavior of the crust and
684 lithosphere could provide further insights into these discrepancies (e.g., Olive et al., 2022).

685

686 6.3 Future applications of our method

687 The success of our method in recovering uplift patterns while rigorously untangling
688 climatic, lithological and tectonic drivers in both synthetic and natural landscapes suggests that
689 it could be applied to other tectonic settings where knowledge of long-term uplift rates is limited.

690 One exciting application of our method is its ability to untangle climatic and tectonic signals,
691 shedding light on the long-standing question of the relative roles of climate and tectonic forcing
692 in the evolution of orogenic regions such as the Andes and Himalayas (e.g., Leonard et al., 2023;
693 Montgomery et al., 2001; Whipple, 2009; Molnar & England, 1990). Our findings indicate that the
694 impact of climate on the section of the Himalayas we studied is relatively negligible (e.g., Godard
695 et al., 2014) as our recovered uplift patterns remained consistent and aligned well with
696 geomorphological indices regardless of climate variability (Fig. 4). Our method could also be
697 applied to explore the effects of potential wetter or drier climatic periods by modifying the
698 climate patterns applied in the inversion. For landscapes with well-established uplift patterns, we
699 could even adapt our approach to invert for long-term climate trends using the same B-spline
700 functions to describe climatic variations.

701 Another compelling application of our method is its ability to recover long-term uplift
702 trends to help constrain seismic hazards along subduction zones, which produce the most
703 destructive earthquakes on Earth. This is particularly relevant in light of recent evidence showing
704 that geodetically locked areas of subduction megathrusts, which produce short-term interseismic
705 surface uplift (e.g., Lindsey et al., 2018; Oryan et al., 2023; Steckler et al., 2016), show systematic
706 correlations with long-term uplift patterns (Fig. 4G) shaped over thousands of years (Jolivet et
707 al., 2020; Malatesta et al., 2021; Saillard et al., 2017). This correlation is even observed in the

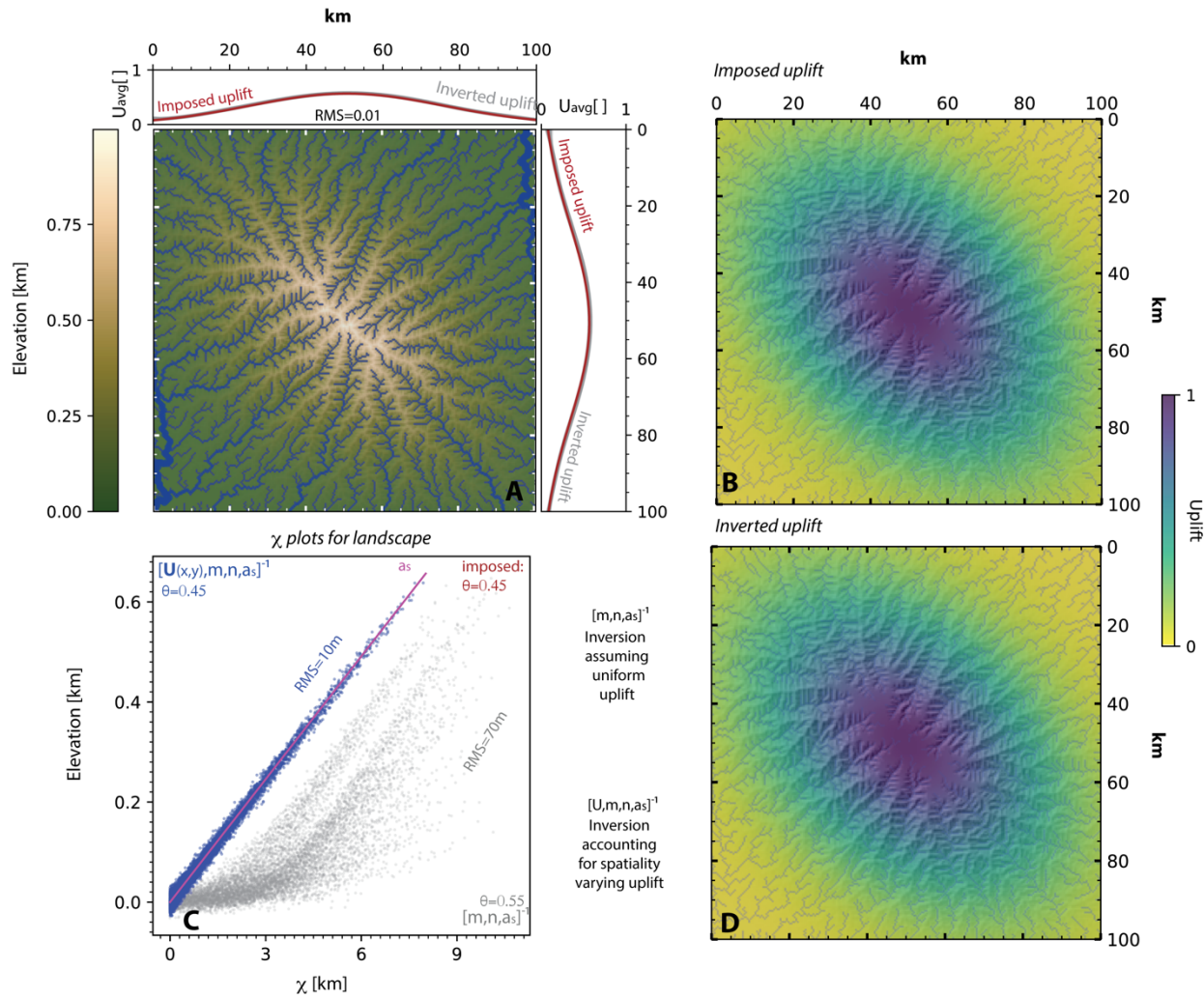
708 Himalayan section we studied (Fig. 4G) and is attributed to the accumulation of irreversible strain
709 during the interseismic period, generating a spatially variable, permanent uplift field recorded by
710 the landscape over many seismic cycles (Oryan et al., 2024). Our inversion method opens the
711 door to leveraging these time-averaged signals captured in landscapes over tens of thousands of
712 years and hundreds of earthquake cycles, offering valuable insights into persistent plate coupling
713 and the associated seismic hazards over extended timescales.

714

715 7 Figures

716

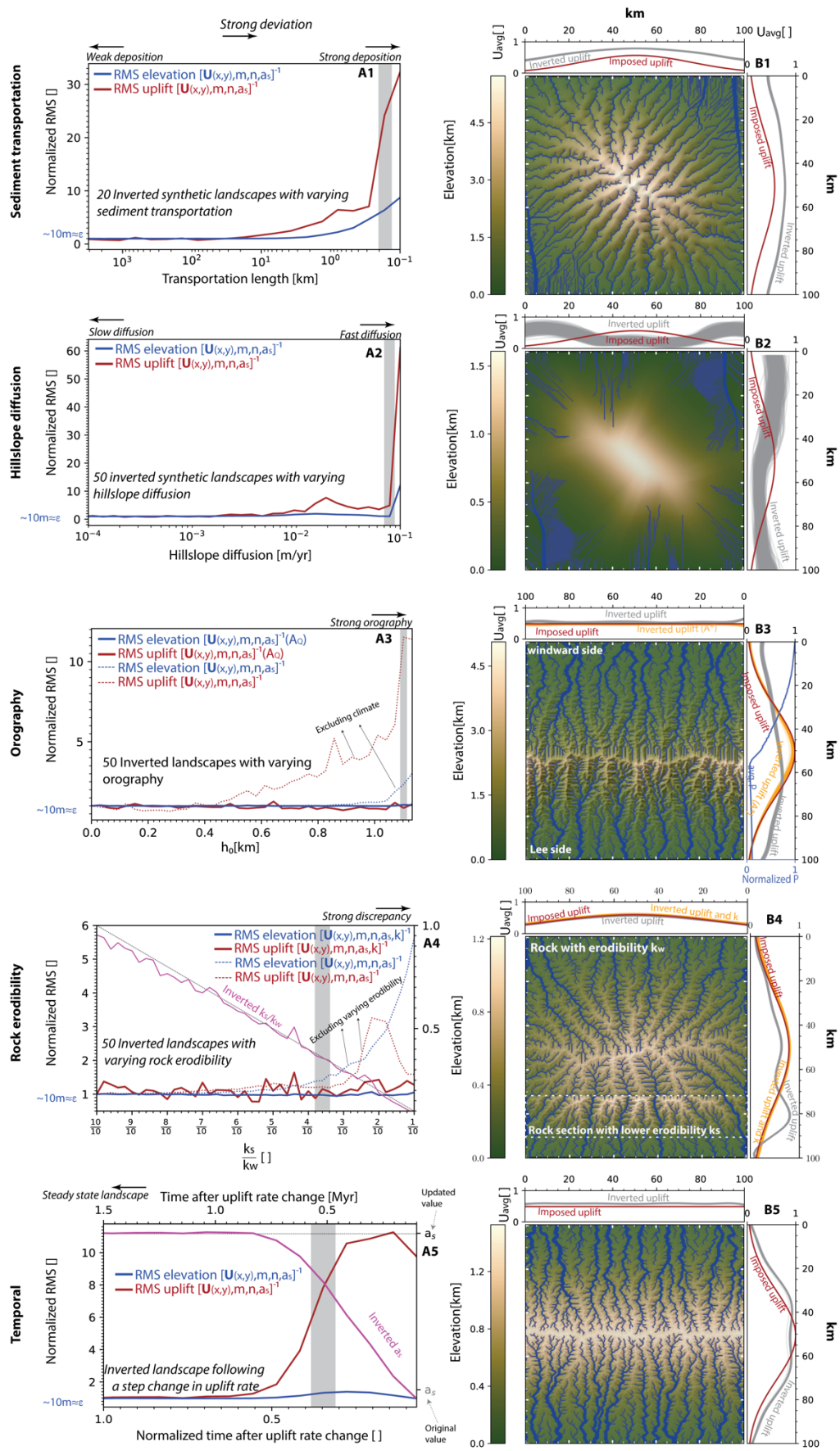
Inversion of detachment limit synthetic landscape



717

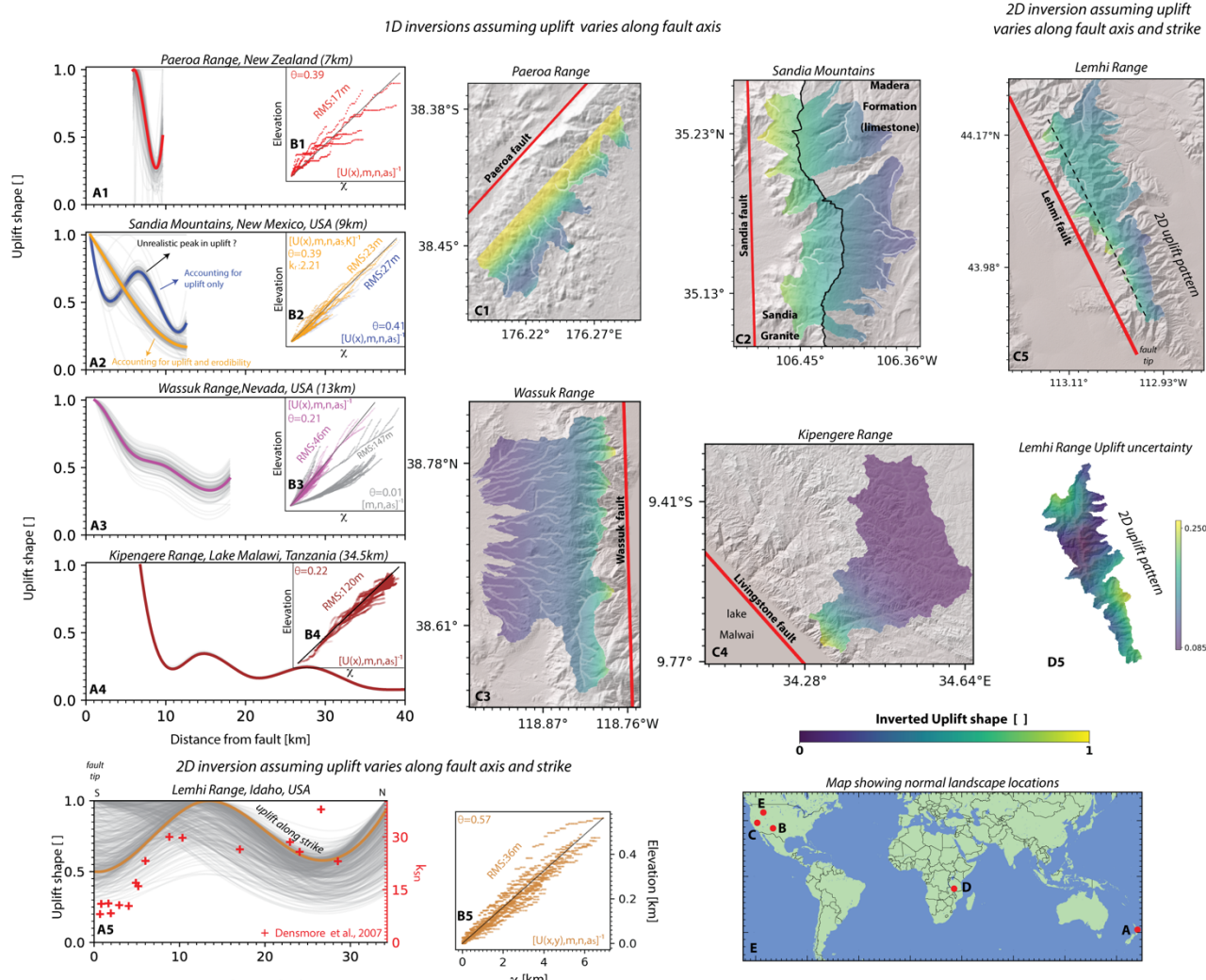
718 **Figure 1 – Inverted detachment limited synthetic landscape.** A – Landscape terrain. Blue dots
 719 show 8000 river nodes used to constrain the inversion with dot size proportional to the drainage
 720 area. Marginal plots show average uplift along axis. Imposed uplift is shown in red curve and 500
 721 samples randomly drawn from the inverted uplift posterior distribution and extrapolated to the
 722 domain are shown in grey. B – Imposed uplift function used during the simulation of the
 723 landscape. Dots show river nodes used in the inversion. C – Points show measured elevation
 724 (z_{obs}) for 8000 river nodes and χ values derived from best inverted solution. Blue and grey
 725 denote inversion results including and excluding uplift, respectively. D – Best inverted uplift
 726 solution extrapolated for the entire domain. Dots mark river nodes used to constrain the
 727 inversion.
 728

Inversion of synthetic landscapes deviating from detachment limited model



730 **Figure 2 – Inverted synthetic landscapes deviating from the detachment limited model showing**
731 **varying degrees of hillslope diffusion (1), sediment deposition(2), orographic effects(3), spatial**
732 **variations in erodibility(4), and temporal changes in uplift rates(5).** A - RMS values for elevation
733 and uplift and normalized with respect to value obtained for the detachment limited landscape
734 (Fig 1). ε denote error we introduced amounting to 10m (See section 4.2). Grey vertical line shows
735 an example landscape described in panel B. B -Landscape Elevation. Blue dots show 8000 river
736 nodes used for the inversion with dot size proportional to the drainage area. Marginal plots show
737 average uplift along axis. Imposed uplift is shown in red curve and 500 samples randomly drawn
738 from the inverted uplift posterior distribution and extrapolated to the domain are shown in grey
739 and orange colors. Panels A4 and A5 show the inverted and imposed parameters k_w/k_s and a_s
740 in magenta and dashed black line, respectively. The x-axis in Panel A5 displays time in million
741 years (top) and as a fraction of the time it takes for the landscape to reach steady state(bottom).
742
743
744
745
746
747
748
749
750
751
752
753
754

Inverted landscapes shaped by normal faults

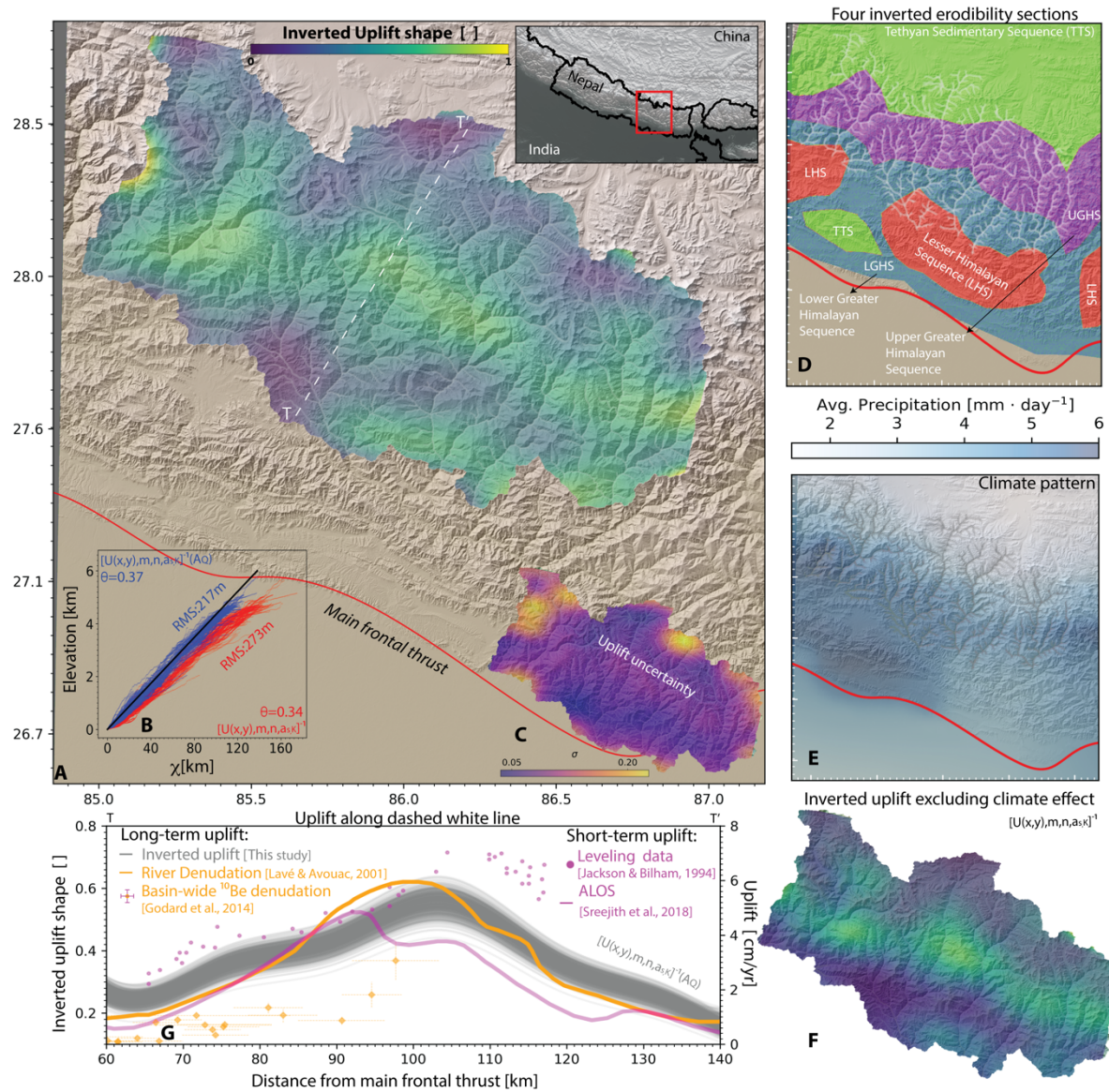


755
756
757
758

Figure 3 – 1D (1-4) and 2D (5) inversions of five natural landscapes shaped by normal faults. A – Best-fitting uplift pattern as a function of distance from the fault is represented by colored curves, with 500 uplift solutions randomly sampled from the posterior distribution shown as grey lines. In A5, the uplift is displayed along strike, following the dashed black line shown in C5. Red markers indicate k_{sn} values computed by Densmore et al. (2007). B - Colored dots represent the χ values for the best-fitting solution for river nodes used in the inversion. Black line marks the inverted slope a_s . Elevation indicates the relief from the base level. The parameter θ denotes the ratio of the inverted m/n values. In A2, k_r shows the erodibility ratio for two inverted rock sections in Sandia. C - The uplift pattern is displayed within the catchments feeding the rivers used in the inversion, highlighted in light white. The fault position is indicated by a red line. In C2, the positions of two lithological sections are shown to the right and left of the ridge line, which is marked by a black line. D – Uplift standard deviation, represented by the colormap, is calculated

771 by evaluating the uplift at each pixel using 500 samples randomly drawn from the posterior
772 distribution. E – map showing landscapes locations.
773

Inverted Himalaya landscape



774
775 **Figure 4 – Inversion results for Himalaya landscape.** A – Best-fitting uplift pattern for the
776 inversion including climate effect is displayed within the catchments feeding the rivers used in
777 the inversion, highlighted by light white dots. White dashed line shows the profile used to plot
778 uplift in panel F. B - Colored dots represent the χ values for the best-fitting solution for river nodes
779 used in the inversion including (blue) and excluding (red) climate effects. Black line marks the
780 best fitting inverted slope a_s . Elevation indicates the relief from the base level. The parameter θ
781 denotes the ratio of the inverted m/n values. C- Uplift standard deviation is calculated by
782 evaluating the uplift at each pixel using 500 samples randomly drawn from the posterior
783 distribution. D – Four distinct lithological sections (Carosi et al., 2018) used to constrain the
784 spatial variability of four inverted erodibility values. River nodes used in the inversion are marked
785 by white dots. E – Average climate pattern used to constrain the climate drainage area, A_Q
786 (section 3.1.4). River nodes used in the inversion are shown by gray dots. F – best fitting uplift

787 pattern for the inversion excluding climate effects. G– Gray curves represent 500 uplift patterns
788 randomly drawn from the posterior distribution along a line perpendicular to the main frontal
789 thrust. Long-term (Godard et al., 2014; Lavé & Avouac, 2001) rates and short-term (Jackson &
790 Bilham, 1994; Sreejith et al., 2018) uplift recorded during the interseismic period are indicated
791 by orange and magenta colors, respectively.

792

793 8 References

- 794 Akaike, H. (1974). A new look at the statistical model identification. *IEEE Transactions on
795 Automatic Control*, 19(6), 716–723. <https://doi.org/10.1109/TAC.1974.1100705>
- 796 Anderson, J. L. (2007). An adaptive covariance inflation error correction algorithm for ensemble
797 filters. *Tellus A: Dynamic Meteorology and Oceanography*, 59(2), 210.
798 <https://doi.org/10.1111/j.1600-0870.2006.00216.x>
- 799 Armijo, R., Meyer, B., King, G. C. P., Rigo, A., & Papanastassiou, D. (1996). Quaternary evolution
800 of the Corinth Rift and its implications for the Late Cenozoic evolution of the Aegean.
801 *Geophysical Journal International*, 126(1), 11–53. [246X.1996.tb05264.x](https://doi.org/10.1111/j.1365-
802 246X.1996.tb05264.x)
- 803 Auzet, A.-V., & Ambroise, B. (1996). Soil Creep Dynamics, Soil Moisture and Temperature
804 Conditions on a Forested Slope in the Granitic Vosges Mountains, France. *Earth Surface
805 Processes and Landforms*, 21(6), 531–542. [https://doi.org/10.1002/\(SICI\)1096-
9837\(199606\)21:6<531::AID-ESP606>3.0.CO;2-B](https://doi.org/10.1002/(SICI)1096-
806 9837(199606)21:6<531::AID-ESP606>3.0.CO;2-B)
- 807 Babault, J., Viaplana-Muzas, M., Legrand, X., Van Den Driessche, J., González-Quijano, M., &
808 Mudd, S. M. (2018). Source-to-sink constraints on tectonic and sedimentary evolution of
809 the western Central Range and Cenderawasih Bay (Indonesia). *Journal of Asian Earth
810 Sciences*, 156, 265–287. <https://doi.org/10.1016/j.jseaes.2018.02.004>
- 811 Bishop, C. M. (2006). *Pattern recognition and machine learning* (Vol. 4). Springer. Retrieved from
812 <https://link.springer.com/book/9780387310732>

- 813 Bontemps, N., Lacroix, P., Larose, E., Jara, J., & Taipe, E. (2020). Rain and small earthquakes
814 maintain a slow-moving landslide in a persistent critical state. *Nature Communications*,
815 11(1), 780. <https://doi.org/10.1038/s41467-020-14445-3>
- 816 Bookhagen, B., & Burbank, D. W. (2010). Toward a complete Himalayan hydrological budget:
817 Spatiotemporal distribution of snowmelt and rainfall and their impact on river discharge.
818 *Journal of Geophysical Research: Earth Surface*, 115(F3).
819 <https://doi.org/10.1029/2009JF001426>
- 820 Campforts, B., Vanacker, V., Herman, F., Vanmaercke, M., Schwanghart, W., Tenorio, G. E., et al.
821 (2020). Parameterization of river incision models requires accounting for environmental
822 heterogeneity: insights from the tropical Andes. *Earth Surface Dynamics*, 8(2), 447–470.
823 <https://doi.org/10.5194/esurf-8-447-2020>
- 824 Carosi, R., Montomoli, C., & Iaccarino, S. (2018). 20 years of geological mapping of the
825 metamorphic core across Central and Eastern Himalayas. *Earth-Science Reviews*, 177,
826 124–138. <https://doi.org/10.1016/j.earscirev.2017.11.006>
- 827 Carretier, S., Martinod, P., Reich, M., & Godderis, Y. (2016). Modelling sediment clasts transport
828 during landscape evolution. *Earth Surface Dynamics*, 4(1), 237–251.
829 <https://doi.org/10.5194/esurf-4-237-2016>
- 830 Castillo, M., Muñoz-Salinas, E., & Ferrari, L. (2014). Response of a landscape to tectonics using
831 channel steepness indices (*ksn*) and OSL: A case of study from the Jalisco Block, Western
832 Mexico. *Geomorphology*, 221, 204–214.
833 <https://doi.org/10.1016/j.geomorph.2014.06.017>

- 834 Cattin, R., & Avouac, J. P. (2000). Modeling mountain building and the seismic cycle in the
835 Himalaya of Nepal. *Journal of Geophysical Research: Solid Earth*, 105(B6), 13389–13407.
836 <https://doi.org/10.1029/2000JB900032>
- 837 Cordonnier, G., Bovy, B., & Braun, J. (2019). A versatile, linear complexity algorithm for flow
838 routing in topographies with depressions. *Earth Surface Dynamics*, 7(2), 549–562.
839 <https://doi.org/10.5194/esurf-7-549-2019>
- 840 Croissant, T., & Braun, J. (2014). Constraining the stream power law: a novel approach combining
841 a landscape evolution model and an inversion method. *Earth Surface Dynamics*, 2(1),
842 155–166. <https://doi.org/10.5194/esurf-2-155-2014>
- 843 Dal Zilio, L., Hetényi, G., Hubbard, J., & Bollinger, L. (2021). Building the Himalaya from tectonic
844 to earthquake scales. *Nature Reviews Earth & Environment*, 2(4), 251–268.
845 <https://doi.org/10.1038/s43017-021-00143-1>
- 846 Davy, P., & Lague, D. (2009). Fluvial erosion/transport equation of landscape evolution models
847 revisited. *Journal of Geophysical Research: Earth Surface*, 114(F3).
848 <https://doi.org/10.1029/2008JF001146>
- 849 Densmore, A. L., Gupta, S., Allen, P. A., & Dawers, N. H. (2007). Transient landscapes at fault tips.
850 *Journal of Geophysical Research*, 112(F3), F03S08.
851 <https://doi.org/10.1029/2006JF000560>
- 852 Ellis, M. A., & Barnes, J. B. (2015). A global perspective on the topographic response to fault
853 growth. *Geosphere*, 11(4), 1008–1023. <https://doi.org/10.1130/GES01156.1>

- 854 Faccenna, C., Glišović, P., Forte, A., Becker, T. W., Garzanti, E., Sembroni, A., & Gvirtzman, Z.
855 (2019). Role of dynamic topography in sustaining the Nile River over 30 million years.
856 *Nature Geoscience*, 12(12), 1012–1017. <https://doi.org/10.1038/s41561-019-0472-x>
- 857 Farr, T. G., Rosen, P. A., Caro, E., Crippen, R., Duren, R., Hensley, S., et al. (2007). The Shuttle
858 Radar Topography Mission. *Reviews of Geophysics*, 45(2).
859 <https://doi.org/10.1029/2005RG000183>
- 860 Fox, M., Goren, L., May, D. A., & Willett, S. D. (2014). Inversion of fluvial channels for paleorock
861 uplift rates in Taiwan. *Journal of Geophysical Research: Earth Surface*, 119(9), 1853–1875.
862 <https://doi.org/10.1002/2014JF003196>
- 863 Gailleton, B., Sinclair, H. D., Mudd, S. M., Graf, E. L. S., & Małenco, L. C. (2021). Isolating Lithologic
864 Versus Tectonic Signals of River Profiles to Test Orogenic Models for the Eastern and
865 Southeastern Carpathians. *Journal of Geophysical Research: Earth Surface*, 126(8),
866 e2020JF005970. <https://doi.org/10.1029/2020JF005970>
- 867 Gailleton, Boris, Mudd, S. M., Clubb, F. J., Grieve, S. W. D., & Hurst, M. D. (2021). Impact of
868 Changing Concavity Indices on Channel Steepness and Divide Migration Metrics. *Journal
869 of Geophysical Research: Earth Surface*, 126(10), e2020JF006060.
870 <https://doi.org/10.1029/2020JF006060>
- 871 Gailleton, Boris, Malatesta, L. C., Cordonnier, G., & Braun, J. (2024). CHONK 1.0: landscape
872 evolution framework: cellular automata meets graph theory. *Geoscientific Model
873 Development*, 17(1), 71–90. <https://doi.org/10.5194/gmd-17-71-2024>

- 874 Godard, V., Bourles, D. L., Spinabella, F., Burbank, D. W., Bookhagen, B., Fisher, G. B., et al. (2014).
- 875 Dominance of tectonics over climate in Himalayan denudation. *Geology*, 42(3), 243–246.
- 876 <https://doi.org/10.1130/G35342.1>
- 877 Goren, L., Fox, M., & Willett, S. D. (2014). Tectonics from fluvial topography using formal linear
- 878 inversion: Theory and applications to the Inyo Mountains, California. *Journal of*
- 879 *Geophysical Research: Earth Surface*, 119(8), 1651–1681.
- 880 <https://doi.org/10.1002/2014JF003079>
- 881 Goren, Liran, Fox, M., & Willett, S. D. (2022). Linear Inversion of Fluvial Long Profiles to Infer
- 882 Tectonic Uplift Histories. In *Treatise on Geomorphology* (pp. 225–248). Elsevier.
- 883 <https://doi.org/10.1016/B978-0-12-818234-5.00075-4>
- 884 Hack, J. T. (1973). *Stream-profile analysis and stream-gradient index*. U.S. Geological Survey.
- 885 Harel, M.-A., Mudd, S. M., & Attal, M. (2016). Global analysis of the stream power law parameters
- 886 based on worldwide ¹⁰Be denudation rates. *Geomorphology*, 268, 184–196.
- 887 <https://doi.org/10.1016/j.geomorph.2016.05.035>
- 888 Hergarten, S., & Robl, J. (2022). The linear feedback precipitation model (LFPM 1.0) – a simple
- 889 and efficient model for orographic precipitation in the context of landform evolution
- 890 modeling. *Geoscientific Model Development*, 15(5), 2063–2084.
- 891 <https://doi.org/10.5194/gmd-15-2063-2022>
- 892 Herman, F., Copeland, P., Avouac, J.-P., Bollinger, L., Mahéo, G., Le Fort, P., et al. (2010).
- 893 Exhumation, crustal deformation, and thermal structure of the Nepal Himalaya derived
- 894 from the inversion of thermochronological and thermobarometric data and modeling of

- 895 the topography. *Journal of Geophysical Research: Solid Earth*, 115(B6).
- 896 <https://doi.org/10.1029/2008JB006126>
- 897 Holtmann, R., Cattin, R., Simoes, M., & Steer, P. (2023). Revealing the hidden signature of fault
- 898 slip history in the morphology of degrading scarps. *Scientific Reports*, 13(1), 3856.
- 899 <https://doi.org/10.1038/s41598-023-30772-z>
- 900 Howard, A. D., & Kerby, G. (1983). Channel changes in badlands. *GSA Bulletin*, 94(6), 739–752.
- 901 [https://doi.org/10.1130/0016-7606\(1983\)94<739:CCIB>2.0.CO;2](https://doi.org/10.1130/0016-7606(1983)94<739:CCIB>2.0.CO;2)
- 902 Huffman, G. J., Bolvin, D. T., Braithwaite, D., Hsu, K., Joyce, R., Xie, P., & Yoo, S.-H. (2015). NASA
- 903 global precipitation measurement (GPM) integrated multi-satellite retrievals for GPM
- 904 (IMERG). *Algorithm Theoretical Basis Document (ATBD) Version*, 4(26), 30.
- 905 Jackson, M., & Bilham, R. (1994). Constraints on Himalayan deformation inferred from vertical
- 906 velocity fields in Nepal and Tibet. *Journal of Geophysical Research: Solid Earth*, 99(B7),
- 907 13897–13912. <https://doi.org/10.1029/94JB00714>
- 908 Jolivet, R., Simons, M., Duputel, Z., Olive, J., Bhat, H. S., & Bletery, Q. (2020). Interseismic loading
- 909 of subduction megathrust drives long term uplift in northern Chile, 1–21.
- 910 <https://doi.org/10.1029/2019GL085377>
- 911 King, G. C. P., Stein, R. S., & Rundle, J. B. (1988). The Growth of Geological Structures by Repeated
- 912 Earthquakes 1. Conceptual Framework. *Journal of Geophysical Research: Solid Earth*,
- 913 93(B11), 13307–13318. <https://doi.org/10.1029/JB093iB11p13307>
- 914 Kirby, E., & Whipple, K. X. (2012). Expression of active tectonics in erosional landscapes. *Journal*
- 915 *of Structural Geology*, 44, 54–75. <https://doi.org/10.1016/j.jsg.2012.07.009>

- 916 Lavé, J., & Avouac, J. P. (2001). Fluvial incision and tectonic uplift across the Himalayas of central
917 Nepal. *Journal of Geophysical Research: Solid Earth*, 106(B11), 26561–26591.
918 <https://doi.org/10.1029/2001JB000359>
- 919 Leonard, J. S., & Whipple, K. X. (2021). Influence of Spatial Rainfall Gradients on River Longitudinal
920 Profiles and the Topographic Expression of Spatially and Temporally Variable Climates in
921 Mountain Landscapes. *Journal of Geophysical Research: Earth Surface*, 126(12),
922 e2021JF006183. <https://doi.org/10.1029/2021JF006183>
- 923 Leonard, J. S., Whipple, K. X., & Heimsath, A. M. (2023). Isolating climatic, tectonic, and lithologic
924 controls on mountain landscape evolution. *Science Advances*, 9(3), eadd8915.
925 <https://doi.org/10.1126/sciadv.add8915>
- 926 Lindsey, E. O., Almeida, R., Mallick, R., Hubbard, J., Bradley, K., Tsang, L. L. H., et al. (2018).
927 Structural Control on Downdip Locking Extent of the Himalayan Megathrust. *Journal of
928 Geophysical Research: Solid Earth*, 123(6), 5265–5278.
929 <https://doi.org/10.1029/2018JB015868>
- 930 Malatesta, L. C., Bruhat, L., Finnegan, N. J., & Olive, J.-A. L. (2021). Co-location of the Downdip
931 End of Seismic Coupling and the Continental Shelf Break. *Journal of Geophysical Research:
932 Solid Earth*, 126(1), e2020JB019589. <https://doi.org/10.1029/2020JB019589>
- 933 Matsuoka, N. (1998). The relationship between frost heave and downslope soil movement: field
934 measurements in the Japanese Alps. *Permafrost and Periglacial Processes*, 9(2), 121–133.
935 [https://doi.org/10.1002/\(SICI\)1099-1530\(199804/06\)9:2<121::AID-PPP281>3.0.CO;2-C](https://doi.org/10.1002/(SICI)1099-1530(199804/06)9:2<121::AID-PPP281>3.0.CO;2-C)
- 936 Meade, B. J. (2010). The signature of an unbalanced earthquake cycle in Himalayan topography?
937 *Geology*, 38(11), 987–990. <https://doi.org/10.1130/G31439.1>

- 938 Merritt, W. S., Letcher, R. A., & Jakeman, A. J. (2003). A review of erosion and sediment transport
939 models. *Environmental Modelling & Software*, 18(8), 761–799.
940 [https://doi.org/10.1016/S1364-8152\(03\)00078-1](https://doi.org/10.1016/S1364-8152(03)00078-1)
- 941 Molnar, P., & England, P. (1990). Late Cenozoic uplift of mountain ranges and global climate
942 change: chicken or egg? *Nature*, 346(6279), 29–34. <https://doi.org/10.1038/346029a0>
- 943 Mortimer, E., Kirstein, L. A., Stuart, F. M., & Strecker, M. R. (2016). Spatio-temporal trends in
944 normal-fault segmentation recorded by low-temperature thermochronology: Livingstone
945 fault scarp, Malawi Rift, East African Rift System. *Earth and Planetary Science Letters*, 455,
946 62–72. <https://doi.org/10.1016/j.epsl.2016.08.040>
- 947 Mudd, S. M., Attal, M., Milodowski, D. T., Grieve, S. W. D., & Valters, D. A. (2014). A statistical
948 framework to quantify spatial variation in channel gradients using the integral method of
949 channel profile analysis. *Journal of Geophysical Research: Earth Surface*, 119(2), 138–152.
950 <https://doi.org/10.1002/2013JF002981>
- 951 Nadai, A. (1963). Theory of flow and fracture of solids. New York, NY: McGraw-Hill. Retrieved
952 from <https://cir.nii.ac.jp/crid/1130282270243960576>
- 953 O'Callaghan, J. F., & Mark, D. M. (1984). The extraction of drainage networks from digital
954 elevation data. *Computer Vision, Graphics, and Image Processing*, 28(3), 323–344.
955 [https://doi.org/10.1016/S0734-189X\(84\)80011-0](https://doi.org/10.1016/S0734-189X(84)80011-0)
- 956 Olive, J.-A., & Behn, M. D. (2014). Rapid rotation of normal faults due to flexural stresses: An
957 explanation for the global distribution of normal fault dips. *Journal of Geophysical
958 Research: Solid Earth*, 119(4), 3722–3739. <https://doi.org/10.1002/2013JB010512>

- 959 Olive, J.-A., Malatesta, L. C., Behn, M. D., & Buck, W. R. (2022). Sensitivity of rift tectonics to global
960 variability in the efficiency of river erosion. *Proceedings of the National Academy of
961 Sciences*, 119(13), e2115077119. <https://doi.org/10.1073/pnas.2115077119>
- 962 Oryan, B., & Buck, W. R. (2020). Larger tsunamis from megathrust earthquakes where slab dip is
963 reduced. *Nature Geoscience*. <https://doi.org/10.1038/s41561-020-0553-x>
- 964 Oryan, B., Betka, P. M., Steckler, M. S., Nooner, S. L., Lindsey, E. O., Mondal, D., et al. (2023). New
965 GNSS and Geological Data From the Indo-Burman Subduction Zone Indicate Active
966 Convergence on Both a Locked Megathrust and the Kabaw Fault. *Journal of Geophysical
967 Research: Solid Earth*, 128(4), e2022JB025550. <https://doi.org/10.1029/2022JB025550>
- 968 Oryan, B., Olive, J.-A., Jolivet, R., Malatesta, L. C., Gailleton, B., & Bruhat, L. (2024). Megathrust
969 locking encoded in subduction landscapes. *Science Advances*, 10(17), eadl4286.
970 <https://doi.org/10.1126/sciadv.adl4286>
- 971 Perron, J. T., & Royden, L. (2013). An integral approach to bedrock river profile analysis. *Earth
972 Surface Processes and Landforms*, 38(6), 570–576. <https://doi.org/10.1002/esp.3302>
- 973 Ponza, A., Pazzaglia, F. J., & Picotti, V. (2010). Thrust-fold activity at the mountain front of the
974 Northern Apennines (Italy) from quantitative landscape analysis. *Geomorphology*, 123(3),
975 211–231. <https://doi.org/10.1016/j.geomorph.2010.06.008>
- 976 Pritchard, D., Roberts, G. G., White, N. J., & Richardson, C. N. (2009). Uplift histories from river
977 profiles. *Geophysical Research Letters*, 36(24). <https://doi.org/10.1029/2009GL040928>
- 978 Robert, X., van der Beek, P., Braun, J., Perry, C., Dubille, M., & Mugnier, J.-L. (2009). Assessing
979 Quaternary reactivation of the Main Central thrust zone (central Nepal Himalaya): New

- 980 thermochronologic data and numerical modeling. *Geology*, 37(8), 731–734.
- 981 <https://doi.org/10.1130/G25736A.1>
- 982 Roberts, G. P., & Michetti, A. M. (2004). Spatial and temporal variations in growth rates along
- 983 active normal fault systems: an example from The Lazio–Abruzzo Apennines, central Italy.
- 984 *Journal of Structural Geology*, 26(2), 339–376. <https://doi.org/10.1016/S0191->
- 985 8141(03)00103-2
- 986 Roering, J. J., Kirchner, J. W., & Dietrich, W. E. (1999). Evidence for nonlinear, diffusive sediment
- 987 transport on hillslopes and implications for landscape morphology. *Water Resources*
- 988 *Research*, 35(3), 853–870. <https://doi.org/10.1029/1998WR900090>
- 989 Roering, J. J., Kirchner, J. W., Sklar, L. S., & Dietrich, W. E. (2001). Hillslope evolution by nonlinear
- 990 creep and landsliding: An experimental study. *Geology*, 29(2), 143.
- 991 [https://doi.org/10.1130/0091-7613\(2001\)029<0143:HEBNCA>2.0.CO;2](https://doi.org/10.1130/0091-7613(2001)029<0143:HEBNCA>2.0.CO;2)
- 992 Rosenbloom, N. A., & Anderson, R. S. (1994). Hillslope and channel evolution in a marine terraced
- 993 landscape, Santa Cruz, California. *Journal of Geophysical Research: Solid Earth*, 99(B7),
- 994 14013–14029. <https://doi.org/10.1029/94JB00048>
- 995 Saillard, M., Audin, L., Rousset, B., Avouac, J.-P., Chlieh, M., Hall, S. R., et al. (2017). From the
- 996 seismic cycle to long-term deformation: linking seismic coupling and Quaternary coastal
- 997 geomorphology along the Andean megathrust. *Tectonics*, 36(2), 241–256.
- 998 <https://doi.org/10.1002/2016TC004156>
- 999 Smith, A. G. G., Fox, M., Moore, J. R., Miller, S. R., Goren, L., Morriss, M. C., & Carter, A. (2024).
- 1000 One Million Years of Climate-Driven Rock Uplift Rate Variation on the Wasatch Fault

- 1001 Revealed by Fluvial Topography. *American Journal of Science*, 324.
- 1002 <https://doi.org/10.2475/001c.92194>
- 1003 Snyder, N. P., Whipple, K. X., Tucker, G. E., & Merritts, D. J. (2000). Landscape response to tectonic
1004 forcing: Digital elevation model analysis of stream profiles in the Mendocino triple
1005 junction region, northern California. *GSA Bulletin*, 112(8), 1250–1263.
1006 [https://doi.org/10.1130/0016-7606\(2000\)112<1250:LRTTFD>2.0.CO;2](https://doi.org/10.1130/0016-7606(2000)112<1250:LRTTFD>2.0.CO;2)
- 1007 Sreejith, K. M., Sunil, P. S., Agrawal, R., Saji, A. P., Rajawat, A. S., & Ramesh, D. S. (2018). Audit of
1008 stored strain energy and extent of future earthquake rupture in central Himalaya.
1009 *Scientific Reports*, 8(1), 16697. <https://doi.org/10.1038/s41598-018-35025-y>
- 1010 Steckler, M. S., Mondal, D. R., Akhter, S. H., Seeber, L., Feng, L., Gale, J., et al. (2016). Locked and
1011 loading megathrust linked to active subduction beneath the Indo-Burman Ranges. *Nature
1012 Geoscience*, 9(8), 615–618. <https://doi.org/10.1038/ngeo2760>
- 1013 Su, Q., Xie, H., Yuan, D.-Y., & Zhang, H.-P. (2017). Along-strike topographic variation of Qinghai
1014 Nanshan and its significance for landscape evolution in the northeastern Tibetan Plateau.
1015 *Journal of Asian Earth Sciences*, 147, 226–239.
1016 <https://doi.org/10.1016/j.jseaes.2017.07.019>
- 1017 Tarantola, A. (2005). *Inverse Problem Theory and Methods for Model Parameter Estimation*.
1018 Society for Industrial and Applied Mathematics.
1019 <https://doi.org/10.1137/1.9780898717921>
- 1020 Taylor, W. J., & Switzer, D. D. (2001). Temporal changes in fault strike (to 90°) and extension
1021 directions during multiple episodes of extension: An example from eastern Nevada. *GSA*

- 1022 *Bulletin*, 113(6), 743–759. <https://doi.org/10.1130/0016->
- 1023 7606(2001)113<0743:TCIFST>2.0.CO;2
- 1024 Watts, A. B. (2001). *Isostasy and Flexure of the Lithosphere*. Cambridge University Press.
- 1025 Retrieved from <https://books.google.com/books?hl=en&lr=&id=QlUgBqJ6m-MC&oi=fnd&pg=PR11&dq=isostasy&ots=KMIwT-K-82&sig=EEBiI2c-910Do0N-5fBlxEyOtq8>
- 1026
- 1027
- 1028 Weissel, J. K., & Karner, G. D. (1989). Flexural uplift of rift flanks due to mechanical unloading of
1029 the lithosphere during extension. *Journal of Geophysical Research: Solid Earth*, 94(B10),
1030 13919–13950. <https://doi.org/10.1029/JB094iB10p13919>
- 1031 Whipple, K. X. (2009). The influence of climate on the tectonic evolution of mountain belts.
1032 *Nature Geoscience*, 2(2), 97–104. <https://doi.org/10.1038/ngeo413>
- 1033 Whipple, K. X., & Tucker, G. E. (1999). Dynamics of the stream-power river incision model:
1034 Implications for height limits of mountain ranges, landscape response timescales, and
1035 research needs. *Journal of Geophysical Research: Solid Earth*, 104(B8), 17661–17674.
1036 <https://doi.org/10.1029/1999JB900120>
- 1037 Willgoose, G., Bras, R. L., & Rodriguez-Iturbe, I. (1991). A physical explanation of an observed link
1038 area-slope relationship. *Water Resources Research*, 27(7), 1697–1702.
1039 <https://doi.org/10.1029/91WR00937>
- 1040 Williams, P. L., & Cole, J. C. (2007). *Geologic Map of the Albuquerque 30' X 60' Quadrangle, North-*
1041 *central New Mexico* (Vol. 2946). US Department of the Interior, US Geological Survey.
- 1042 Retrieved from
1043 <https://books.google.com/books?hl=en&lr=&id=SmHuAAAAMAAJ&oi=fnd&pg=PA1&dq>

1044 =Geologic+Map+of+the+Albuquerque+30%E2%80%99+x+60%E2%80%99+Quadrangle,+
1045 North-Central+New+Mexico&ots=XjNI3pAW57&sig=zlxdaGlePxXrpviuYPt1dkoxExo
1046 Wobus, C., Whipple, K. X., Kirby, E., Snyder, N., Johnson, J., Spyropoulos, K., et al. (2006). Tectonics
1047 from topography: Procedures, promise, and pitfalls. In S. D. Willett, N. Hovius, M. T.
1048 Brandon, & D. M. Fisher (Eds.), *Tectonics, Climate, and Landscape Evolution* (Vol. 398, p.
1049 0). Geological Society of America. [https://doi.org/10.1130/2006.2398\(04\)](https://doi.org/10.1130/2006.2398(04))
1050 Yanites, B. J., Tucker, G. E., Mueller, K. J., Chen, Y.-G., Wilcox, T., Huang, S.-Y., & Shi, K.-W. (2010).
1051 Incision and channel morphology across active structures along the Peikang River, central
1052 Taiwan: Implications for the importance of channel width. *GSA Bulletin*, 122(7–8), 1192–
1053 1208. <https://doi.org/10.1130/B30035.1>
1054
1055

1056 9 Funding

1057
1058 This work was funded by the Emergence(s)–Ville de Paris Program Project “Inelasticity in the
1059 Subduction earthquake cycle” (J.-A.O.); the French Agence Nationale de la Recherche (ANR) grant
1060 GeoSigMA (J.-A.O.), the European Research Council (ERC) under the European Union’s horizon
1061 2020 research and innovation program, Geo-4d project, grant agreement 758210 (R.J.); institut
1062 Universitaire de France (R.J.); h2020 european Research council, grant no. 803721 (B.G.);
1063 Chateaubriand Fellowship Program ,Green Postdoctoral Scholarship from IGPP at SiO and
1064 national Science Foundation, grant no. nSF-OAc- 2311208 (B.O.)

1065

1066

1067 10 Supplementary information

1068

1069 **Text S1 – B Splines**

1070

1071 The B-spline function we used in parametrizing the uplift are described as follow (De Boor,
1072 1978; Piegl & Tiller, 1997):

1073
$$1. U(x) = \sum_i^{i+d} Q_i B_{i,d}(x)$$

1074 Where Q_i is the spline coefficient controlling the behavior of the B-spline basis function of
1075 order d , $B_{i,d}(x)$, defined recursively in the following way:

1076
$$2. B_{i,0}(x) = \begin{cases} 1, & x \in [t_i, t_{i+1}] \\ 0, & \text{elsewhere} \end{cases}$$

1077
$$B_{i,d}(x) = \frac{x - t_i}{t_{i+d} - t_i} B_{i,d-1}(x) + \frac{t_{i+d+1} - x}{t_{i+d+1} - t_{i+1}} B_{i+1,d-1}(x)$$

1078

1079 t_i is the position of node i .

1080

1081 To describe a two-dimensional uplift patterns we rely on a convolution of B-spline basis
1082 function to describe a surface (De Boor, 1978; Piegl & Tiller, 1997):

1083

1084
$$3. U(x,y) = \sum_i^{n+d} \sum_j^{j+d} Q_{i,j} B_{i,d}(x) B_{j,d}(y)$$

1085

1086 To compute our uplift function, we distribute nodes along a rectangle uniform grid with
1087 constant spacing along the x and y axis. This enables us to adopt a simpler and computationally
1088 efficient form of B-spline basis (Agrapart & Batailly, 2020). For 1D cubic solution where uplift
1089 varies along the x-axis we use:

1090

1091
$$4. U(x) = \frac{1}{6} [u_i^3 \ u_i^2 \ u_i \ 1] \cdot R \cdot \begin{bmatrix} Q_i \\ Q_{i+1} \\ Q_{i+2} \\ Q_{i+3} \end{bmatrix}$$

1092

1093 For the 2D case where uplift pattern is a function of x and y we use:

1094

1095
$$5. \quad U(x, y) = \frac{1}{36} [v_j^3 \ v_j^2 \ v_j \ 1] \cdot R \cdot \begin{bmatrix} Q_{i,j} & Q_{i+1,j} & Q_{i+2,j} & Q_{i+3,j} \\ Q_{i,j+1} & Q_{i+1,j+1} & Q_{i+2,j+1} & Q_{i+3,j+1} \\ Q_{i,j+2} & Q_{i+1,j+2} & Q_{i+2,j+2} & Q_{i+3,j+2} \\ Q_{i,j+3} & Q_{i+1,j+3} & Q_{i+2,j+3} & Q_{i+3,j+3} \end{bmatrix} R^t \begin{bmatrix} \mu_i^3 \\ \mu_i^2 \\ \mu_i \\ 1 \end{bmatrix}$$

1096

1097 Where $\mu_i = \frac{x-t_i}{t_{i+1}-t_i}$, $v_j = \frac{y-t_j}{t_{j+1}-t_j}$ and $R = \begin{bmatrix} -1 & 3 & -3 & 1 \\ 3 & -6 & 3 & 0 \\ -3 & 0 & 3 & 0 \\ 1 & 4 & 1 & 0 \end{bmatrix}$.

1098

1099 We note that the numbers of parameters needed is nodes+d(=3) and as we are only interested
1100 in the shape of uplift and normalize our uplift solution between 0 and 1.

1101 Finally, we highlight that our recovered uplift is constrained only by river nodes within our
1102 rectangular domain defining the b-spline surface. Nonetheless, we can extrapolate the uplift
1103 surface across the entire B-spline domain using these parameters. We consider that the
1104 recovered uplift applies only to the basins that feed our selected river nodes, as the water flowing
1105 through these influence the information they provide.

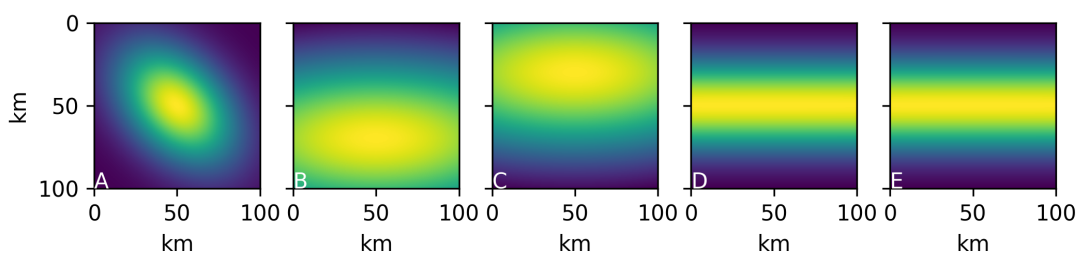
1106

1107

Cases	x_0 [km]	y_0 [km]	σ_x [km]	σ_y [km]	θ []	Illustration Fig.
Detachment limited, Sediment transportation, Hillslope diffusion (Fig. 1 ,2 and 3)	50	50	30	20	45	1,S2A
Temporal uplift shape (South ridge uplift function ; Fig 5)	50	70	100	40	0	S2B
Temporal change (North ridge uplift function ; Fig 5)	50	30	100	40	0	S2C
Climatic effect & Temporal uplift rate (Figs. 5 & 3)	50	50	1000	20	0	S2D
Erodibility ratio (Fig 6)	50	50	40	25	0	S2E

1108 Table S1 – Imposed tectonic uplift used in synthetic landscape. Uplift functions illustrations are
 1109 shown in Fig. S1.

1110



1111

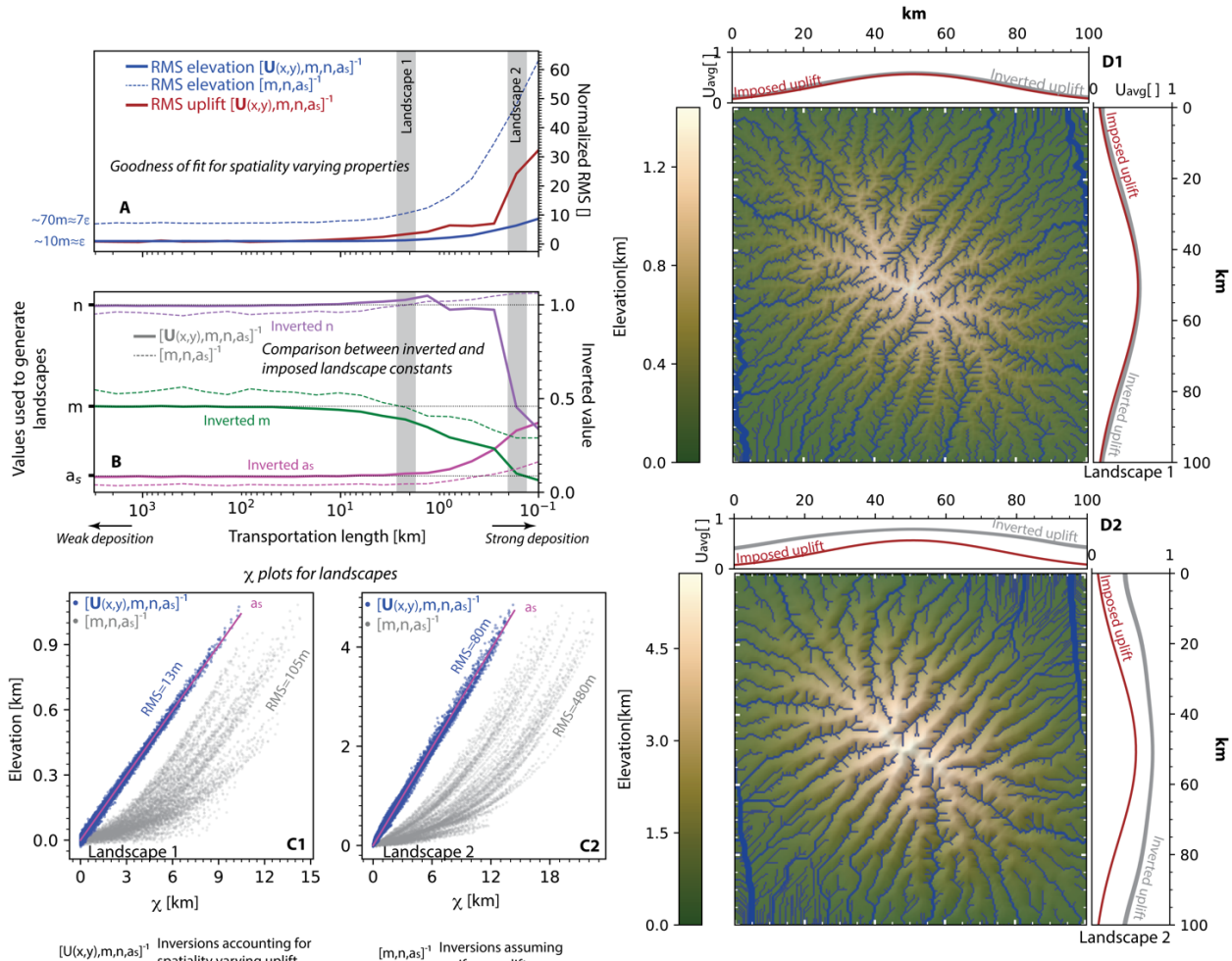
1112

1113

1114

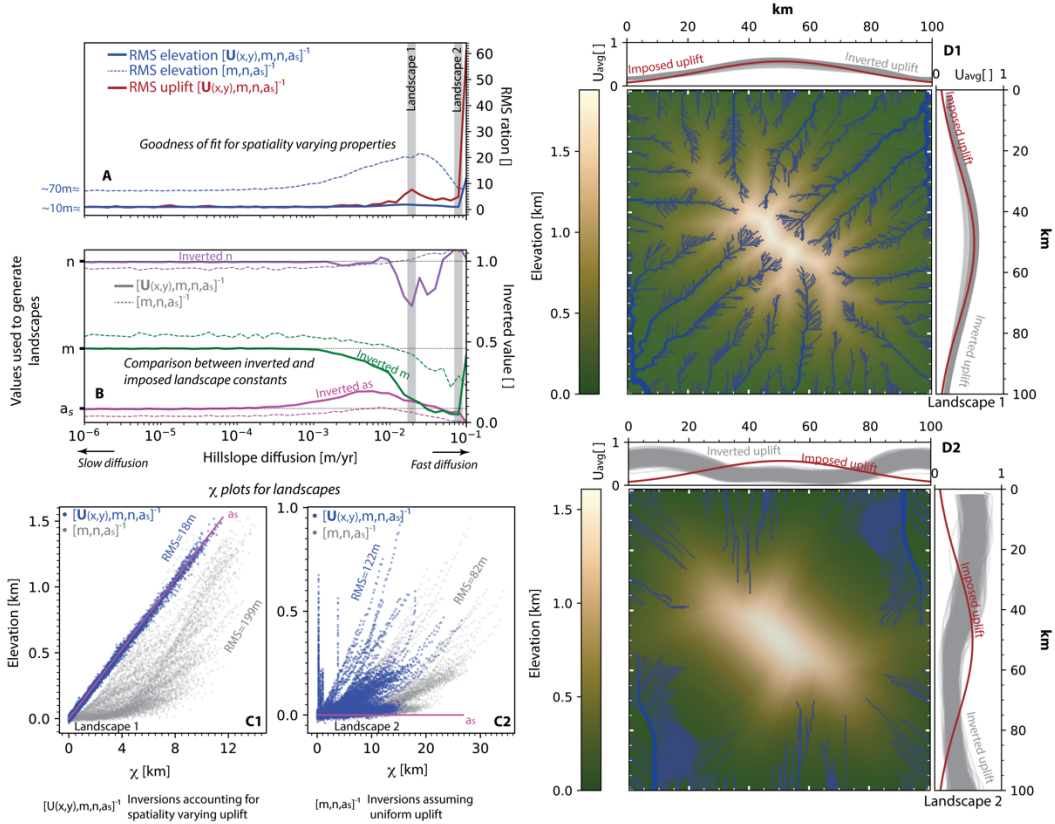
Fig S1 – Uplift imposed for synthetic landscapes cases (see table S1).

Inverted synthetic landscapes with various degrees of sediment transportation and deposition



1115
 1116 **Figure S2 – Inverted synthetic landscapes with various degrees of sediment transportation and**
 1117 **deposition.** Panels A and B show comparison between imposed and recovered landscape
 1118 properties for inversions of 50 synthetic landscapes, each characterized by a distinct simulated
 1119 deposition value. A – RMS values for elevation and uplift and normalized with respect to value
 1120 obtained for the landscape with the weakest deposition. ε denote error we introduced
 1121 amounting to 10m (See section 4.2). B – Comparison between imposed (black dash curve) and
 1122 mean inverted and m , n and a_s values. Continuous and dashed curves denote inversion results
 1123 including and excluding uplift, respectively. Grey vertical lines show two landscapes described in
 1124 panels C and D. C – Points show elevation for 8000 river nodes and χ values derived from best
 1125 inverted solution. Blue and grey denote inversion results including and excluding uplift,
 1126 respectively. D – Landscapes Elevation. Blue dots show 8000 river nodes used for the inversion
 1127 with dot size proportional to the drainage area. Marginal plots show average uplift along axis.
 1128 Imposed uplift is shown in red curve and 500 samples randomly drawn from the inverted uplift
 1129 posterior distribution and extrapolated to the domain are shown in grey.
 1130

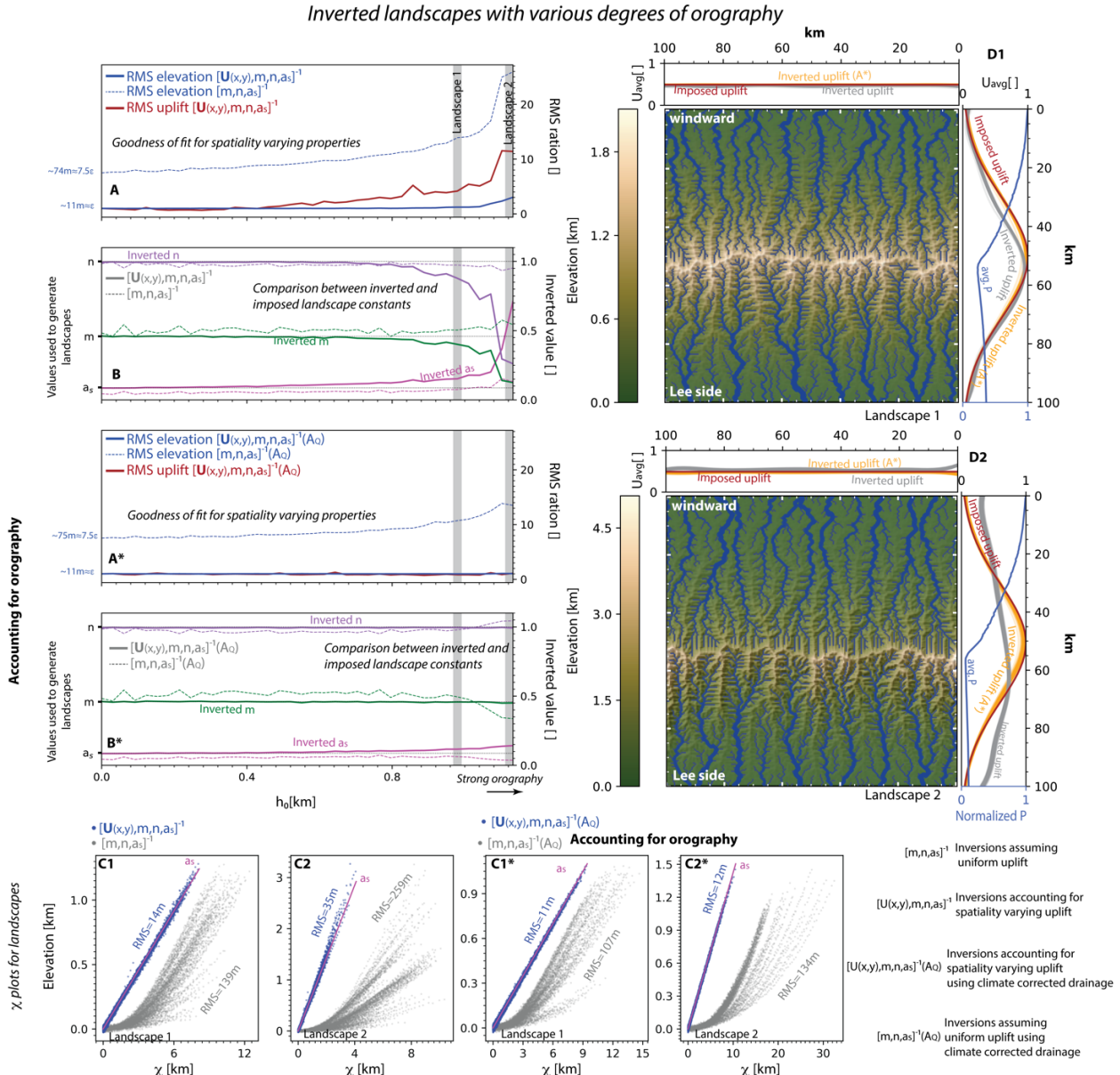
Inverted synthetic landscapes with various degrees of hillslope diffusion

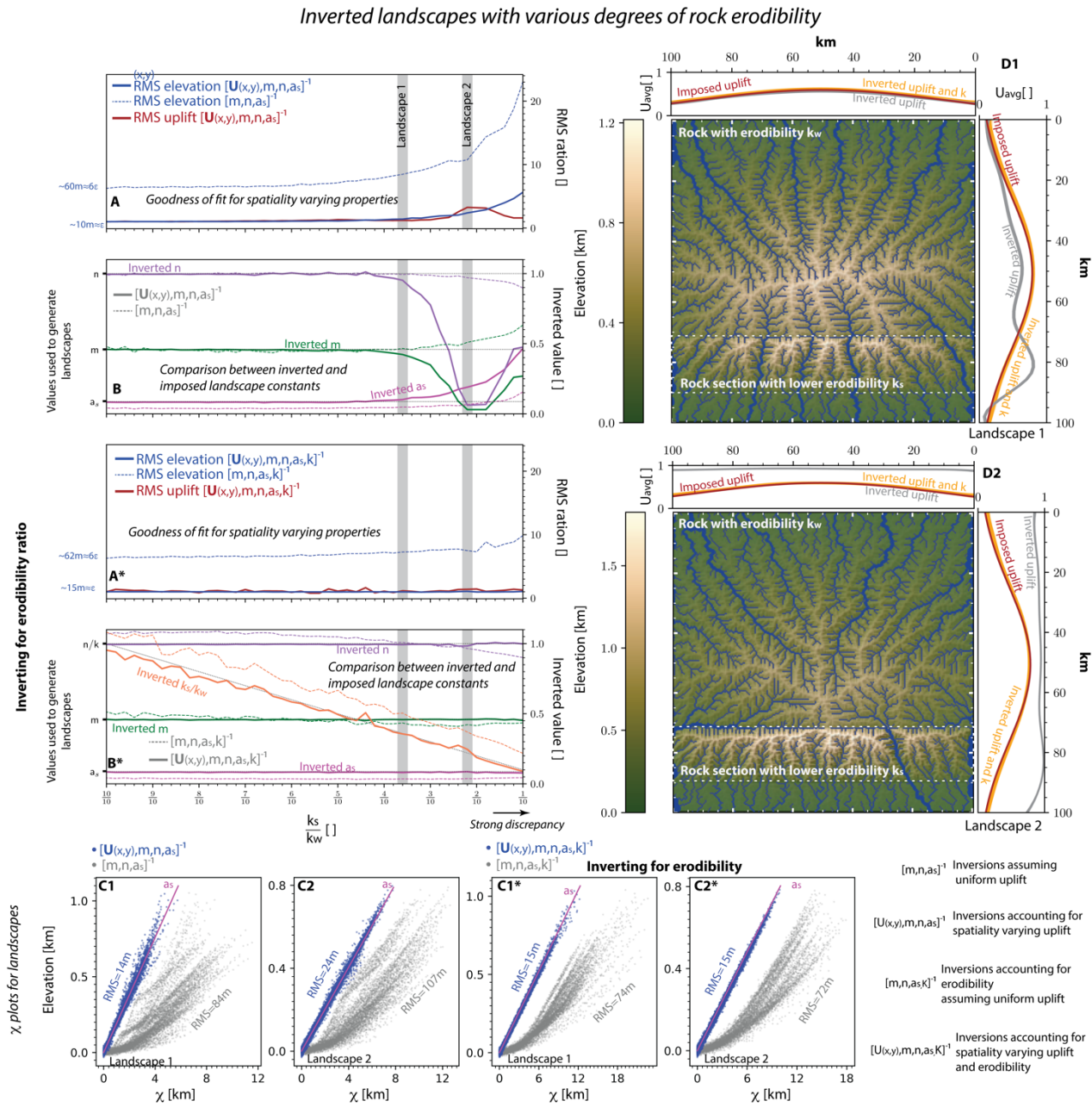


1131

1132 **Figure S3 – Inverted synthetic landscapes with various degrees of hillslope diffusion.**

1133 Panels A,A*,B and B* show comparison between imposed and recovered landscape properties
 1134 for inversions of 50 synthetic landscapes, each characterized by a distinct h_o (See section 4.3.5).
 1135 Panels with and without an * show outputs for inversions including and excluding the effect of
 1136 orographic perception on drainage area, respectively. Blue curves in marginal plots in panels D1
 1137 and D2 show the averaged perception along the x axis where 1 and 0 indicate large and negligible
 1138 perception, respectively. See Fig. S2 for complete figure description.
 1139
 1140





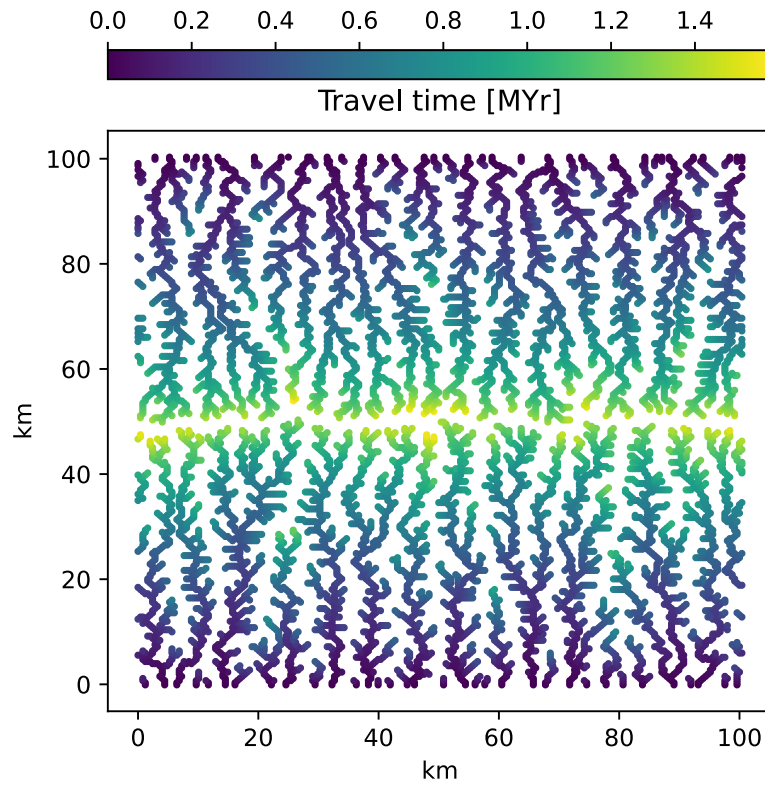
1152
1153

1154

1154
1155
1156
1157
1158
1159
1160

1160

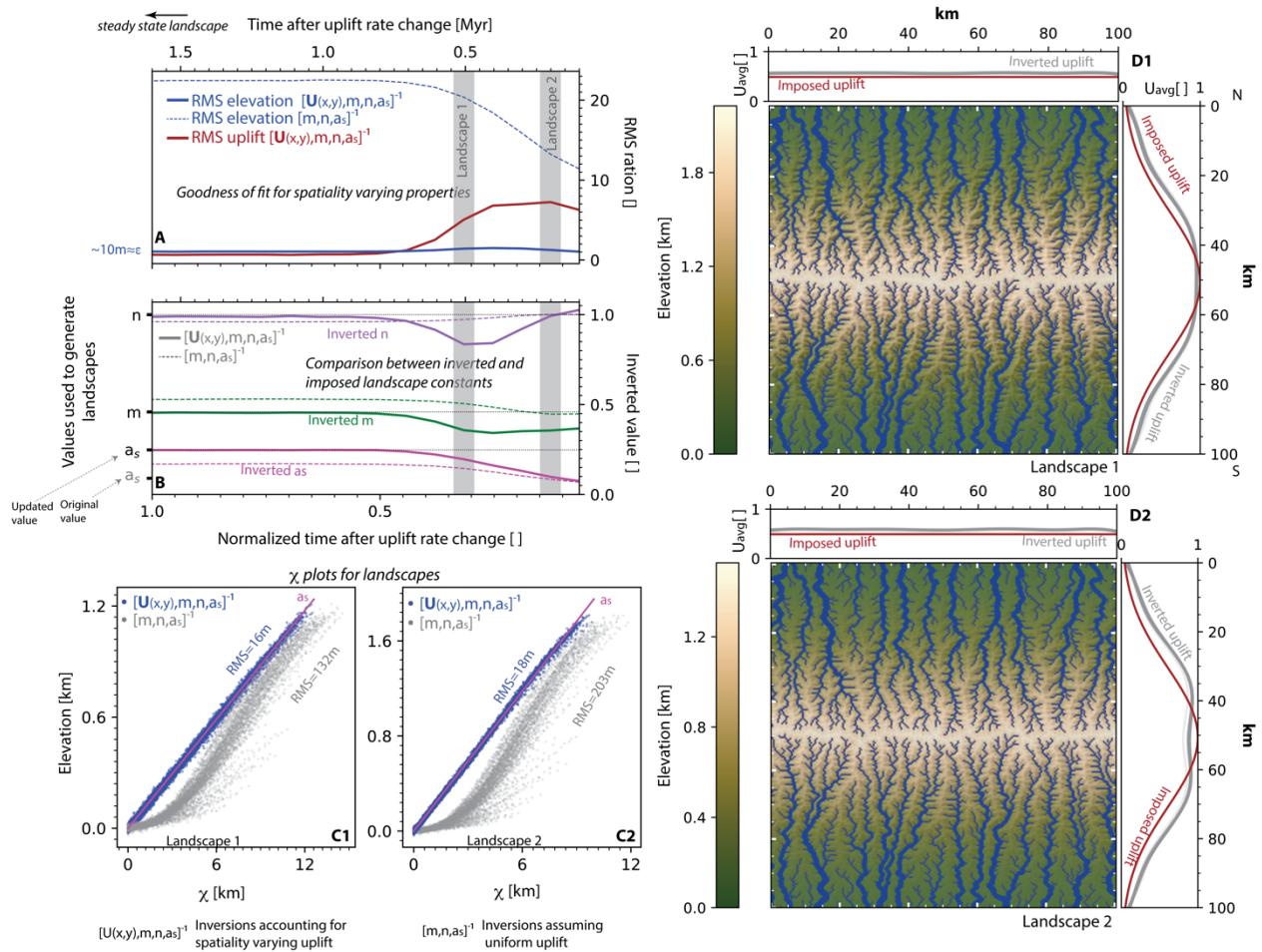
1161
1162



1163
1164
1165
1166

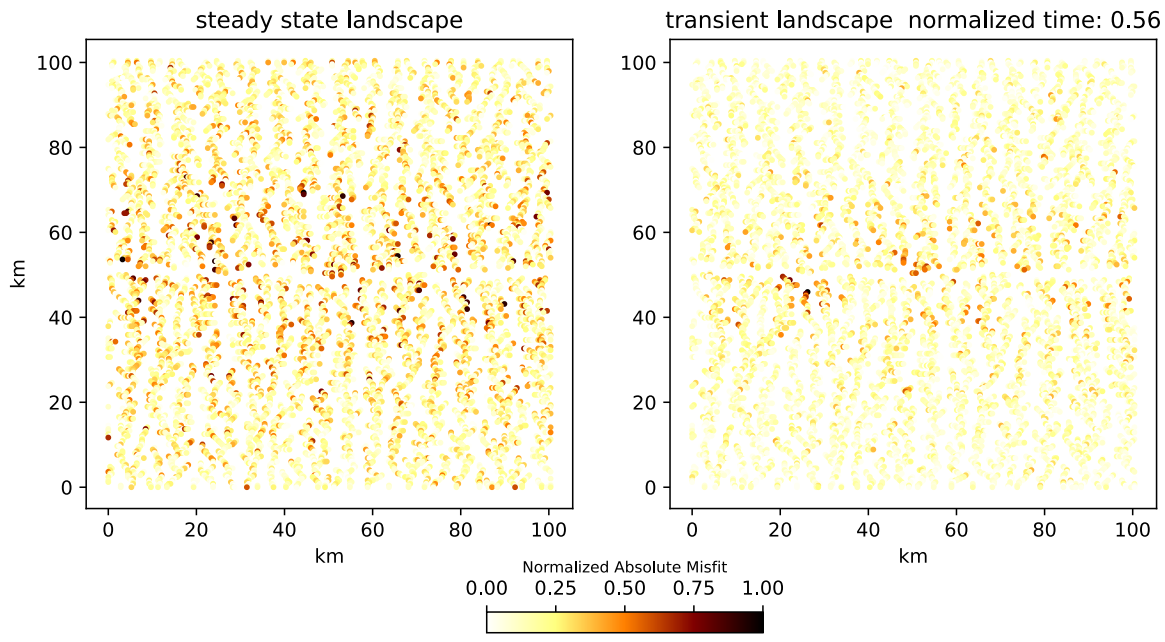
Fig S6—knickpoint travel time from base level to river node.

Inverted landscape following a step change in uplift rate



1167
1168
1169
1170
1171
1172
1173
1174

Figure S7 – Inverted synthetic landscape following an instantaneous change in uplift rate.
Panels A and B show comparison between imposed and recovered landscape properties for inversions of snapshots of the landscape at intervals of 0.1 Myr following the step change. Results are presented in time normalized with respect to the duration the landscape requires to reach steady state. See Fig. S2 for complete figure description.



1175
 1176 Fig S8 – Elevation misfit for two synthetic landscapes. The largest misfit values for the transient
 1177 landscape are concentrated upstream around the river tips, which have not yet reached
 1178 equilibrium. In contrast misfits are almost evenly distributed across steady state landscape.
 1179
 1180

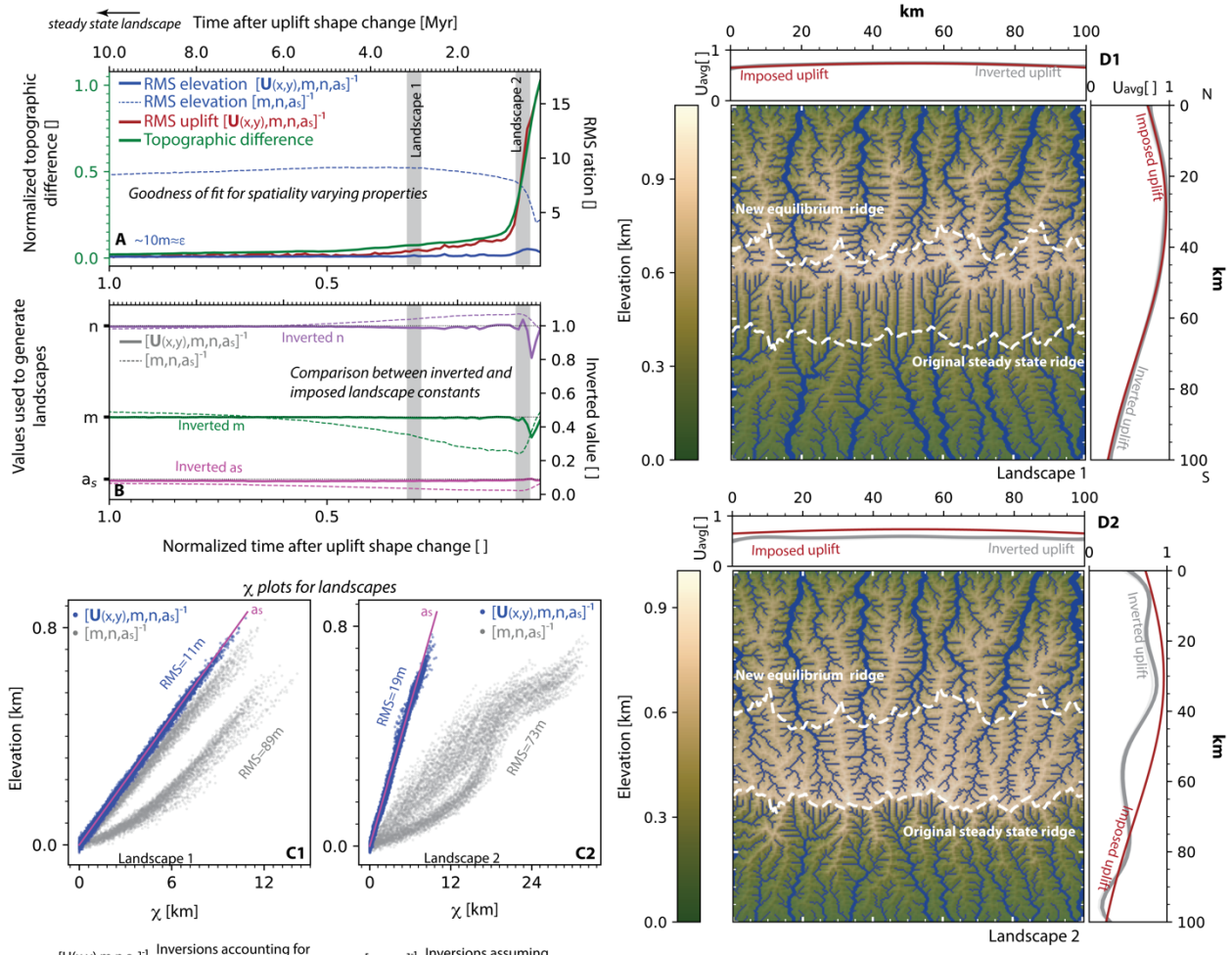
1181 **Text S2 – Synthetic landscape subject to temporal changes in uplift pattern**

1182
1183 For completeness we examine the effect of temporal changes in uplift pattern (under
1184 constant uplift rate) and simulate a detachment-limited landscape in equilibrium, characterized
1185 by a well-formed east-west mountain range along the southern end of the domain (Fig. 5; Table
1186 S1; Fig. S1). We then introduce a step change in the uplift pattern, resulting in a ~30 km slow
1187 migration of the mountain ridge towards the north (Fig. S9; Table S1; Fig. S1). Following this
1188 instantaneous change, we continue simulating the landscape for an additional 10 million years,
1189 performing inversions on landscape snapshots recorded at intervals of 0.1 million years.

1190 Due to the nonlinearity and complexity of the signal we introduce (Royden & Taylor
1191 Perron, 2013; Steer, 2021), we estimate the time for the landscape to reach a new equilibrium
1192 by computing the mean of the absolute differences in topographic height across successive
1193 timesteps (green curve, Fig. S9A). Approximately 10 million years following the step change, the
1194 ridge stabilizes at its final position, with mean topographic change diminishing to about 1% of its
1195 maximum value post-change (Fig. S9A).

1196 The inverted and recorded elevations align almost perfectly, while other landscape
1197 properties show more pronounced errors (Figs. S9A & S9B). This consistency in elevation retrieval
1198 suggests that the inversion effectively compensates with adjustments in other parameters to
1199 return accurate elevation values. This is because the transient signals are primarily driven by
1200 detachment-limited processes, in contrast to sediment deposition and hillslope diffusion. This
1201 illustrates the challenge of determining whether a natural landscape, lacking direct constraints
1202 on uplift and landscape constants, is in steady state based solely on elevation errors. Additional
1203 similarity with scenario (1) is that the recovered uplift almost perfectly matches the imposed
1204 uplift by about half the dimensionless time, significantly earlier than when the landscape reaches
1205 its final equilibrium. This is particularly notable given that the ridge still needs to migrate
1206 approximately 10 km before reaching its steady state position (Figs. S9D1 & S9D2).

Inverted landscape following a step change in uplift shape



1207

$[U(x,y),m,n,as]^{-1}$ Inversions accounting for

1208

spatially varying uplift

1209

Figure S9 – Inverted synthetic landscape following an instantaneous change in uplift shape.

1210

Panels A and B show comparison between imposed and recovered landscape properties for inversions of snapshots of the landscape at intervals of 0.1 Myr following the step change. Results are presented in time normalized with respect to the duration the landscape requires to reach steady state. Green curve shows the normalized mean topographic difference computed between successive timesteps. Dashed white lines show the original and new positions of the ridge in steady state. See Fig. 2 for complete figure description.

1211

1212

1213

1214

1215

1216

1217

1218

1219 Table S2 – Properties of natural landscapes. *Olive et al., 2022 and references therein. **Ellis &
 1220 Barnes, 2015 and references therein. ^ See text S5.

1221

	Base altitude for χ [m]	Min drainage area [km^2]	Master fault UTM coordinates (x_1, y_1) and (x_2, y_2) (m) + UTM zone *	Knots Used for inversion	Brittle layer thickness[km]*	$u_0 [\frac{mm}{yr}]$	Age of onset [Myr]
Paeroa Range, New Zealand (A)	400	2.5	(4.3843e5, 5.7567e6) (4.3115e5, 5.7487e6) UTM 60H	1	6-8	1.5**	1-0.9**
Sandia Mountains, New Mexico, USA (B)	2100	2	(3.6423e5, 3.8973e6) (3.6452e5, 3.8866e6) UTM 13N	1	7-10	0.14^	22^
Wassuk Range, Nevada, USA (C)	1500	1	(3.4679e5, 4.2762e6) (3.4620e5, 4.2968e6) UTM 11S	4	11-14	0.6**	15**
Kipengere Range / N.E. shores of Lake Malawi, Tanzania (D)	550	1	(6.1128e5, 8.9515e6) (6.6862e5, 8.8871e6) UTM 36L	7	32-37	0.12^	23^
Lemhi Range, Idaho, USA (E)	2200	3	(2.6519e5, 4.9486e6) (2.875e5, 4.9305e6) UTM 12T	Kx=2 ky=3	12-16	0.5**	6.5**
Himalayas	550	10	UTM 45N	Kx=9; ky=9			

1222

1223 **Text S2 - Akaike Information Criterion**

1224

1225 The Akaike Information Criterion is a method used in statistics to determine the relative quality

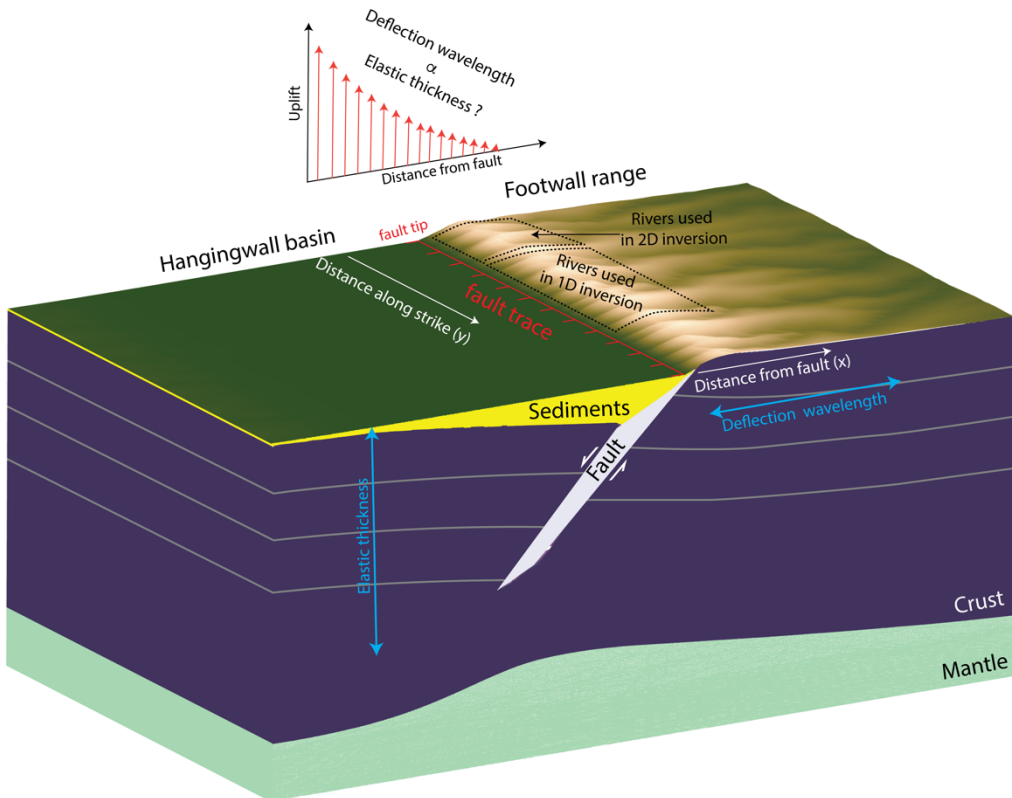
1226 of statistical models for a given set of data. It is calculated using the formula:

1227
$$AIC = 2(k - \ln(L))$$

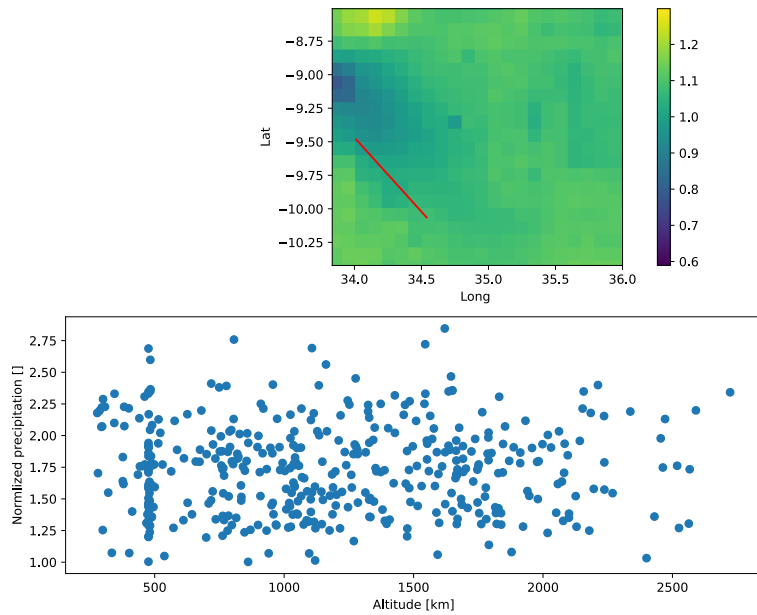
1228 where k is the number of parameters in the model and L is the maximum value of the likelihood

1229 function for the model.

1230



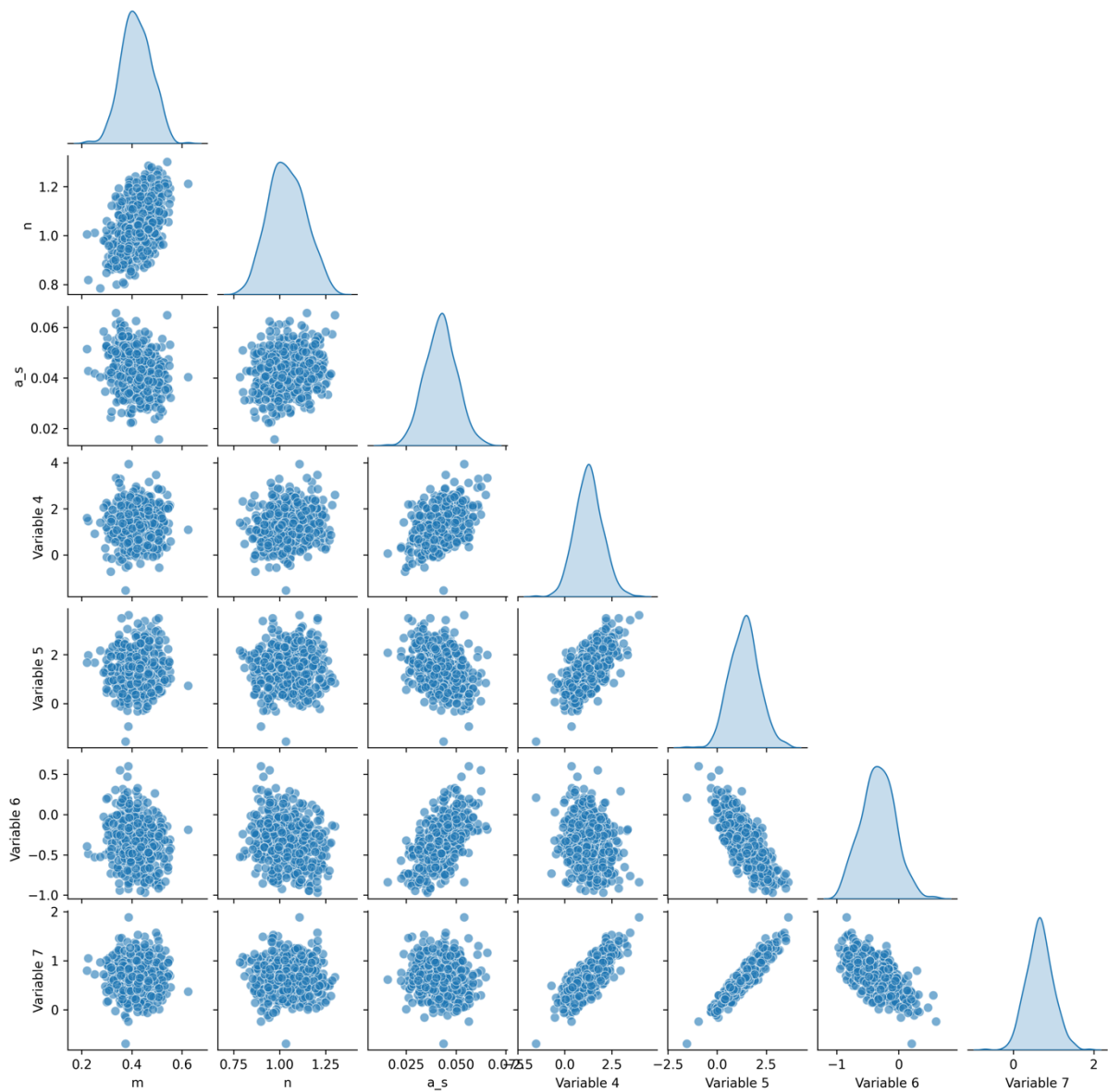
1231
 1232
 1233
 1234 Figure S10 – Illustration showing the deflation of the lithosphere and resulting landscape due to
 1235 offset accommodated along a half graben normal fault system.
 1236



1237
 1238 Fig S11 – Upper panel – Standard deviation of precipitation divided by the average precipitation
 1239 per pixel for rainfall data collected over 23 years from November 1, 2000, by the GPM mission
 1240 (Huffman et al., 2015). The red line indicates the position of the Livingston normal fault (Fig S8).
 1241 Lower panel - Elevation and average precipitation for 418 data points corresponding to the
 1242 rainfall data shown in the upper panel.
 1243

1244

NZ



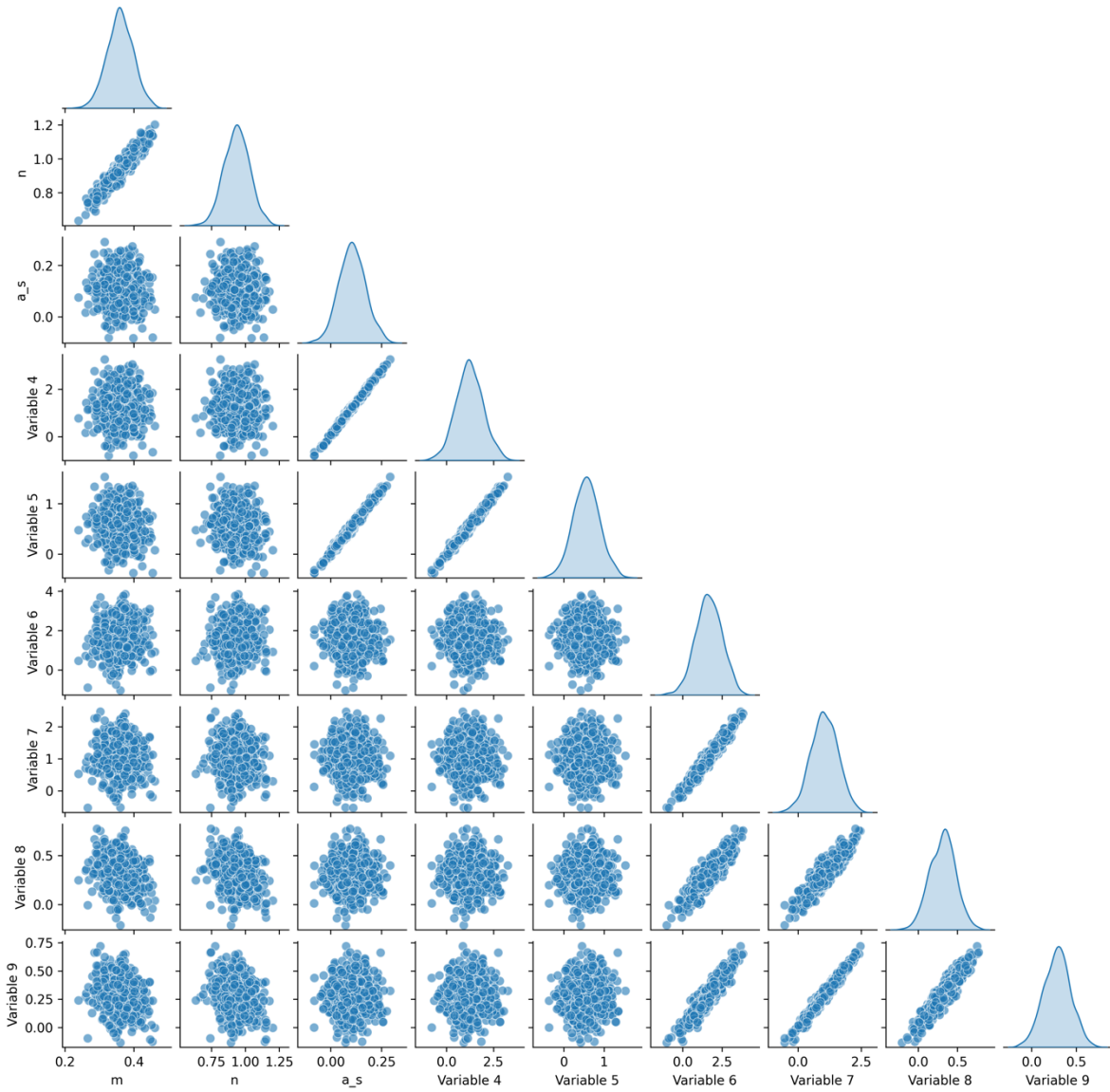
1245

1246 Figure S12 - Pair plots for the New Zealand landscape. Variables 4-7 indicate parameters

1247 controlling the b-spline functions. These were estimated using 500 samples randomly drawn

1248 from the posterior distribution.

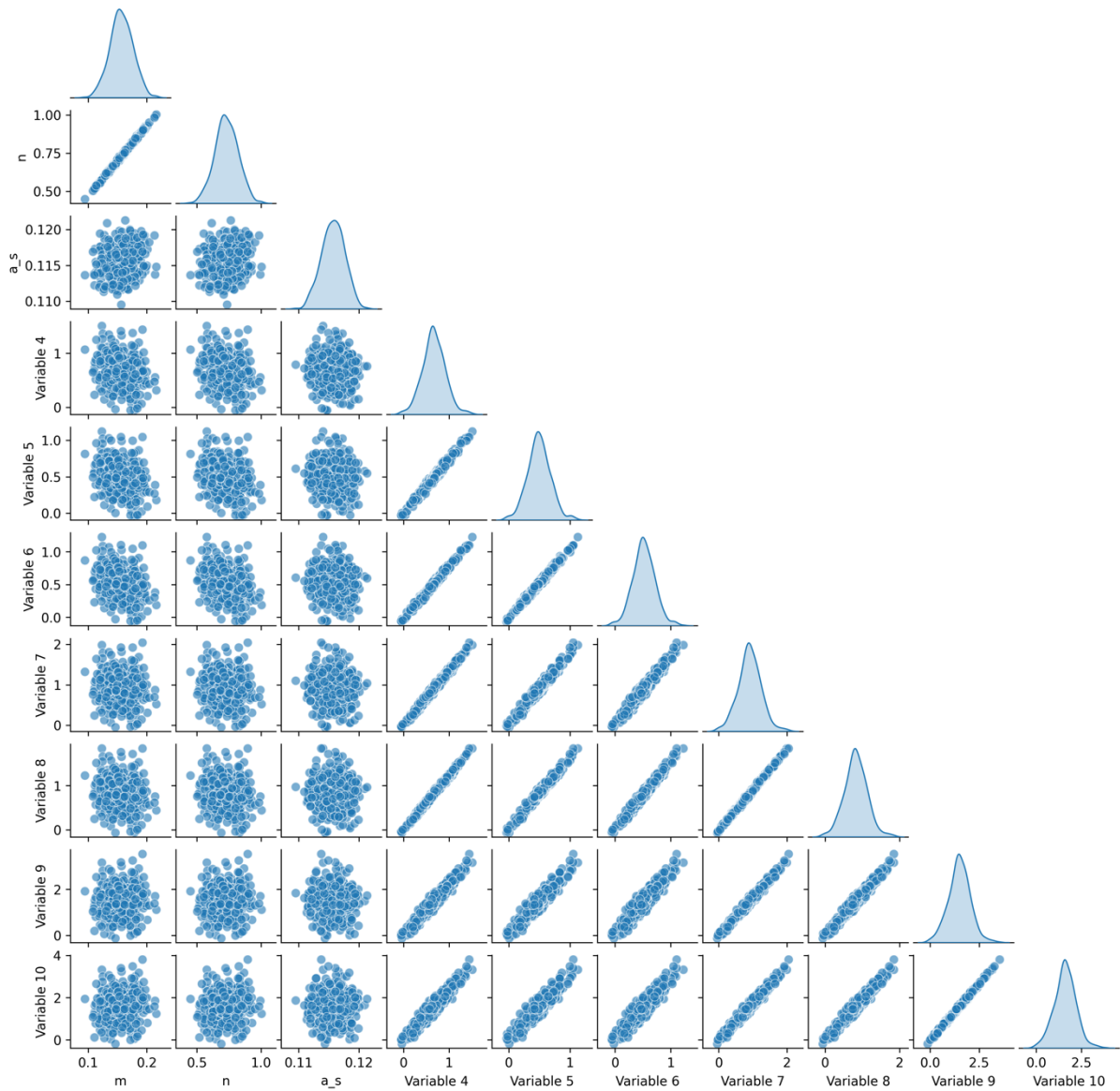
Sandia



1249

1250 Figure S13 - Pair plots for the Sandia landscape. Variables 4-5 and 6-9 indicate parameters
1251 controlling the erodibility and b-spline functions, respectively. These were estimated using 500
1252 samples randomly drawn from the posterior distribution.

Wassuk



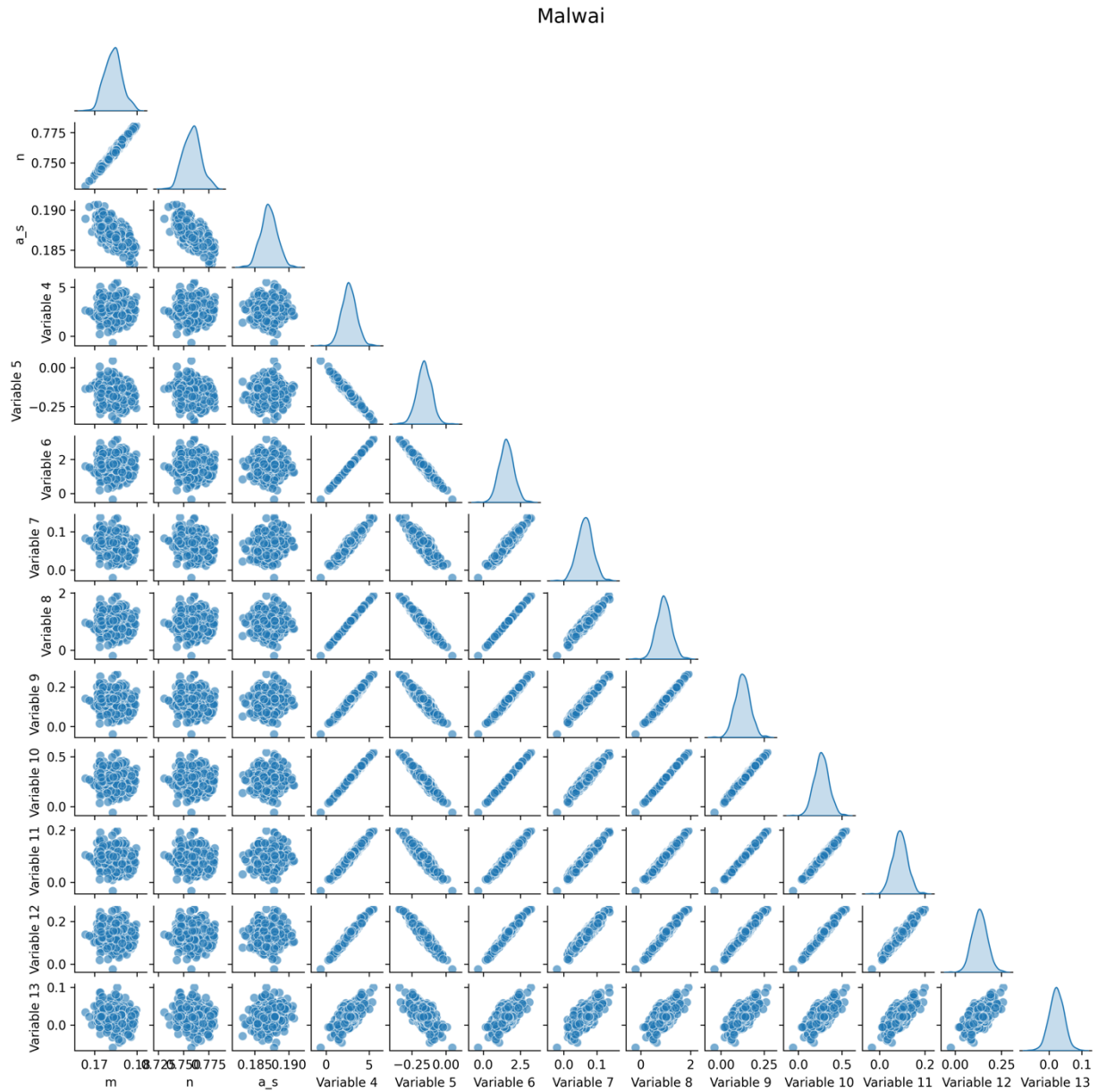
1253

1254

1255

1256

Figure S14 - Pair plots for the Wassuk landscape. Variables 4-10 indicate parameters controlling the b-spline functions. These were estimated using 500 samples randomly drawn from the posterior distribution.

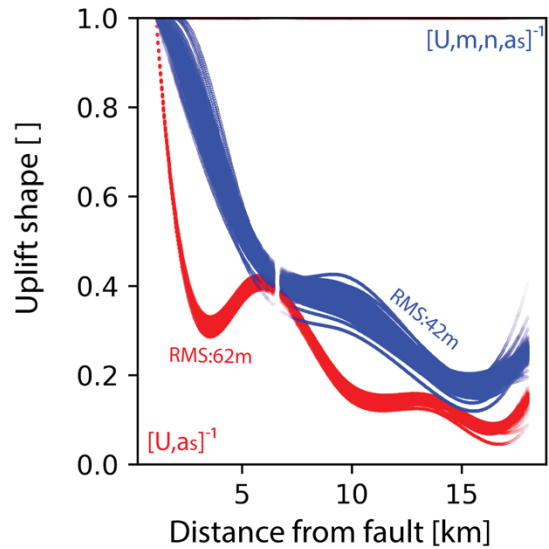


1257

1258 Figure S15 - Pair plots for the Malwai landscape. Variable 4-13 indicate parameters controlling
 1259 the b-spline functions. These were estimated using 500 samples randomly drawn from the
 1260 posterior distribution.

1261

1262



1263
1264 Fig S16 – Comparison of uplift solutions for Wassuk Range for the case the inversion is fixed at
1265 m=0.45 and n=1. Colored curve show 500 uplift solutions randomly sampled from our posterior
1266 distributions.
1267

	Tethyan Sedimentary Sequence (TTS)	Upper Himalayan Sequence (UGS)	Greater Himalayan Sequence (LHS)	Lesser Himalayan Sequence (LGHS)	Lower Himalayan Sequence (LGHS)
Relative erodibility value	0.88 ± 0.40	1.19 ± 0.54	1.01 ± 0.46	0.87 ± 0.39	

1269 Table S3 – Best-fitting and standard deviation of relative erodibility values for the Himalayan
 1270 inversion including the climate effect.

1272 **Text S3 – Furter exploration of temporally varying uplift rates**

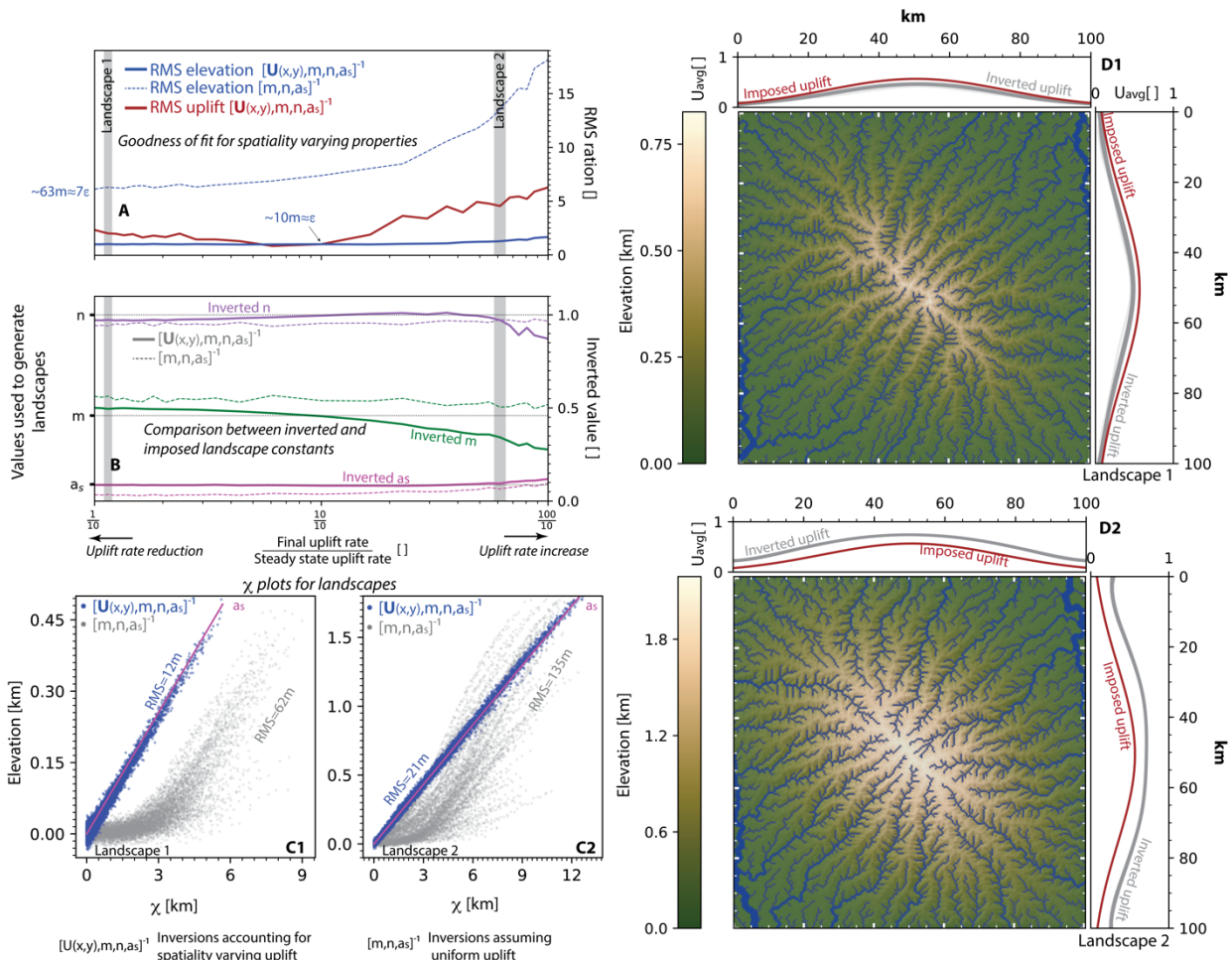
1273
1274 To investigate the impact of variable uplift rates, we modeled 29 landscapes, each initially
1275 at steady state under a uniform uplift rate of 1.2 mm/year. We then simulated each landscape
1276 over an additional 400K years, during which uplift rates linearly adjusted to final values between
1277 12 and 0.12 mm/year (Fig. S12). This 400K-year period is designed to reflect the fastest changes
1278 in uplift rate recorded along Utah's Wasatch Fault (Smith et al., 2024). Throughout this time
1279 interval, we retained and inverted 12 landscape snapshots, allowing us to assess the temporal
1280 variation in landscape response. The results we present are averaged from these 12 landscape
1281 analyses.

1282 Our inversion reveals that greater contrasts in uplift rates lead to pronounced deviations
1283 from the imposed landscape properties. For instance, a tenfold increase in uplift rate results in
1284 RMS values ranging from 3 to 7 times larger than the baseline (Fig. S12). Notably, landscapes
1285 experiencing an increase in uplift rate exhibit RMS values approximately twice as large as those
1286 undergoing a decrease (Fig. S12A). This difference likely stems from the landscape's delayed
1287 response in adjusting to reduced rock removal at lower uplift rates. The erodibility of the rock
1288 affects this asymmetry, with higher erodibility potentially reversing the trend. Despite less
1289 precision with significant uplift increases, the inversion still accurately captures the uplift pattern,
1290 albeit with a slight, consistent deviation from the imposed configuration (Figs. S12D1 & S12D2).

1291

1292

Inverted synthetic landscapes with various degrees of uplift rate change



1293
1294

1295 **Figure S17 – Inverted synthetic landscapes with varying degrees of temporal changes in**
1296 **imposed tectonic uplift rate.** Panels A and B show comparison between imposed and recovered
1297 landscapes properties for inversions of 50 synthetic landscapes, each characterized by a distinct
1298 final uplift rate value employed in simulating the landscape. Values shown in panels A and B are
1299 averaged for 12 snapshots of the landscape during the 400K years over which the change in rate
1300 occurred. Panels C & D show the results for the last time step of the tectonic rate change. See
1301 Fig. 2 for complete figure description.

1302
1303

1304

1305 **Text S4 – Furter exploration of temporally varying uplift shape**

1306

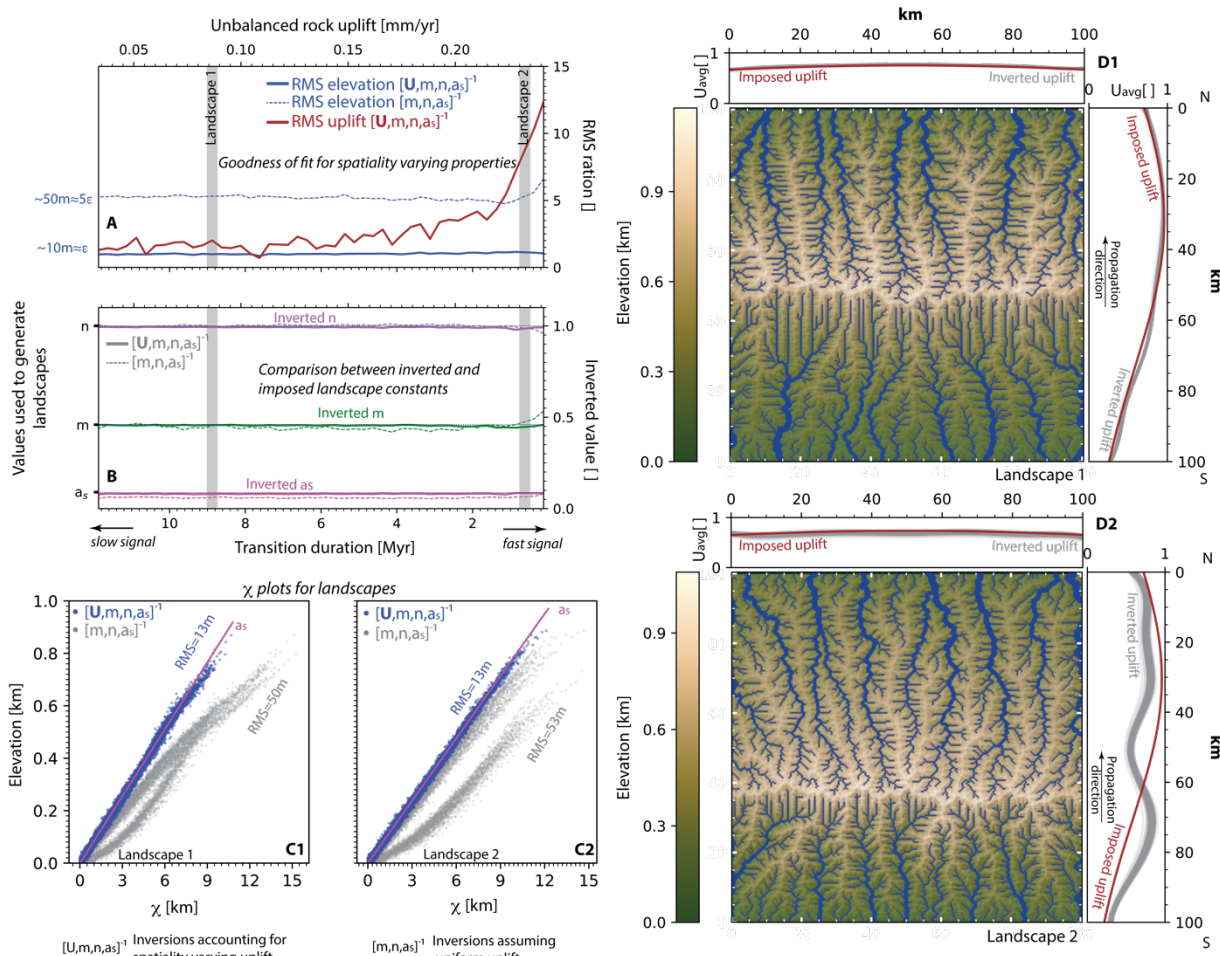
1307

1308 We modeled 48 landscapes that initially reach a topographic steady state, featuring an
1309 uplifting domain along the southern edge of the model (Table S1; Fig. S1). We then reduce uplift
1310 rate along the southern edge while commensurably increasing it along the northern edge,
1311 causing the mountain range to migrate north (e.g., Fig S13D1). Each landscape is associated with
1312 a distinct migration period ranging 120K to 12 M years (Figs. S13 & S1; Table S1). We report the
1313 average results for retained 12 snapshots of each landscape intervals during this migration
1314 process.

1315 The inversion results in realistic inversion outputs with elevation RMS values only a few
1316 meters higher than ε when the timescale of tectonic changes is ≥ 6 Myr (Figs. S13A, S13B &
1317 S13D1). In contrast, faster temporal changes, which build synthetic topography at rate of at least
1318 $0.17 \text{ mm} \cdot \text{yr}^{-1}$ results in inverted uplift showing increasingly larger deviation from imposed
1319 uplift (Figs S13A & S13B).

1320

Inverted landscapes with various degrees of transient uplift pattern



1321

Figure S18 – Inverted synthetic landscapes subject to varying temporal changes in the imposed tectonic uplift pattern. Panels A and B show comparison between imposed and recovered landscape properties for inversions of 50 synthetic landscapes, each characterized by a distinct duration of north migrating uplift signal value. Values shown in panels A&B are averaged for 12 snapshots of the landscape during the migration processes while panels C & D show the results for the last time step of the tectonic migration. See Fig. 2 for complete figure description.

1322

1323

1324

1325

1326

1327

1328

1329

1330

1331 **Text S5 – Estimating k_0 and knickpoint travel time**

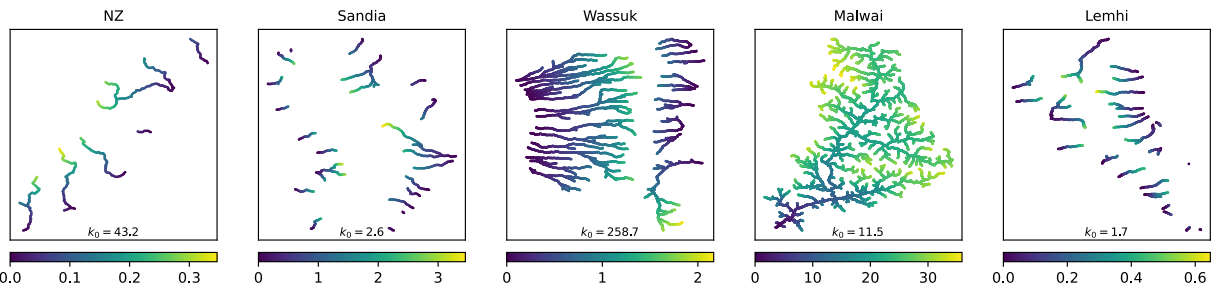
1332 We use our inverted m, n, a_s and previous estimations of u_o (Table S2; Ellis & Barnes, 2015) to
1333 retrieve k_0 using $k_0 = \frac{u_0}{a_s^n A_0^m}$. For Lake Malawi and Sandia landscapes, where direct uplift rate
1334 estimations are unavailable, we follow Ellis & Barnes (2015) and estimate the minimum uplift
1335 rate using timing of fault initiation and a linear scaling relationship between fault displacement
1336 and length (Schlische et al., 1996)

1337 Lake Malawi and the Kipengere Range, known as the Livingstone Mountains, have formed
1338 due to flexural-isostatic rebound in response to localized extension at the southern end of the
1339 East African Rift. High-resolution seismic imaging of sediments deposited in the northern basin
1340 of Lake Malawi along the ~80km long Livingstone Fault, the focus of our analysis, suggests a fault
1341 displacement (throw) of between 6.6 and 7.4 km. (Accardo et al., 2018). Apatite
1342 thermochronology along the Livingstone fault system indicates that regional cooling, associated
1343 with the onset of Cenozoic rifting, started approximately 23 million years ago (Mortimer et al.,
1344 2016). This results in uplift rate of $0.12 \text{ mm} \cdot \text{yr}^{-1}$.

1345 The Sandia fault delineates the steep western face of the Sandia Mountains and marks
1346 the eastern boundary of the Albuquerque basin part of the Rio Grande Rift. Apatite fission track
1347 (AFT) and (U-Th)/He data from the Sandia Mountains indicate fault activity and rapid cooling 22-
1348 17Ma (House et al., 2003). Using fault length of 100km (McCalpin & Harrison, 2006) we estimate
1349 minimum uplift rate of $0.14 \text{ mm} \cdot \text{yr}^{-1}$.

1350 Finally, we use equation (3) to compute knickpoint travel time from the base level (Fig. S13). We
1351 would like to note that we calculate the drainage pattern assuming a uniform precipitation rate
1352 of $1 \text{ m} \cdot \text{yr}^{-1}$, which is generally a reasonable value except for the Sandia and Wassuk regions
1353 where rainfall is lower. However, we disregard this effect as these landscapes are in a steady
1354 state, and lowering the uniform precipitation rate would reduce A_0 , leading to even faster travel

1355 times.



1356
1357 Fig S19 – Travel time in million years for the five natural landscapes used in the study. Colormap
1358 shows travel time from river base. k_0 shows 10^{-6} erodibility values.
1359

1360

1361 **Text S6 – Estimating deflection wavelength**

1362

1363 Theory

1364

1365 The deflection of a broken thin elastic plate overlying a viscous half space subject to kilometer
1366 long offset is expressed as (Nadai, 1963):

1367

$$1. \quad w(x) = w_0 \cdot \exp\left(-\frac{x}{\alpha_b}\right) \cdot \cos\left(\frac{x}{\alpha_b}\right)$$

1368 Where w_0 is the deflection at the fault axis, x distance from the fault, and α_b is the flexure
1369 wavelength:

1370

1371

$$2. \quad \alpha_b = \alpha_0 T_e^{\frac{3}{4}}$$

1372 Where α_0 coefficient linking deflection wavelength and the elastic plate thickness, T_e , and is often
1373 expressed as:

1374

1375

$$3. \quad \alpha_0 = \left(\frac{E}{3(\rho_m - \rho_c) \cdot g(1 - \nu^2)} \right)^{\frac{1}{4}}$$

1376

1377 Where E is Young's modulus, g gravity, ν Poisson's ratio and ρ_m and ρ_c are the densities of the
1378 viscous layers and elastic layers, respectively.

1379

1380

1381 Estimating α_0 from our inverted 1D uplift profile

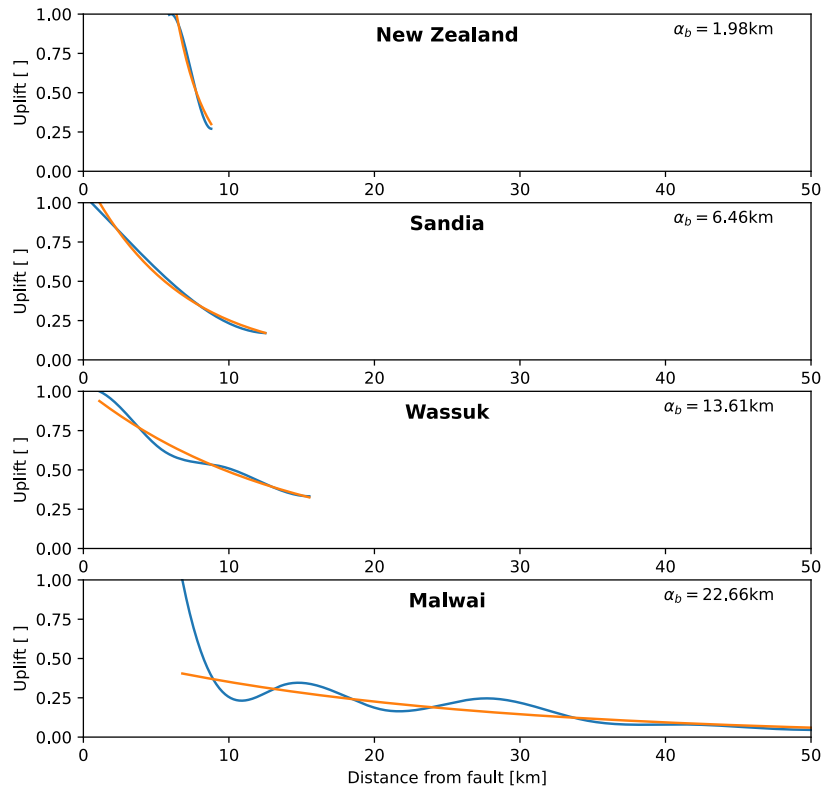
1382

1383 To estimate α_b for each landscape we used our inverted 1D uplift profiles and fitted it
 1384 with a simplified version of equation (1): $u(x) = w_o \cdot e^{\frac{-x}{\alpha_b}}$ (Fig. S15). We then fitted equation (2)
 1385 and found $\alpha_0 = 1.2 \text{ km}^{1/4}$ (Fig. S16). Assuming $E = 30 \text{ GPa}$, $\nu = 0.25$ and $\rho_m - \rho_c = 300 \frac{\text{kg}}{\text{m}^3}$
 1386 yield $\alpha_0 = 43.6 \text{ km}^{1/4}$. Lastly, we note that we utilized Python's scipy module relying on non-
 1387 linear least squares to fit the data shown in this section (Vugrin et al., 2007).

1388

1389

1390



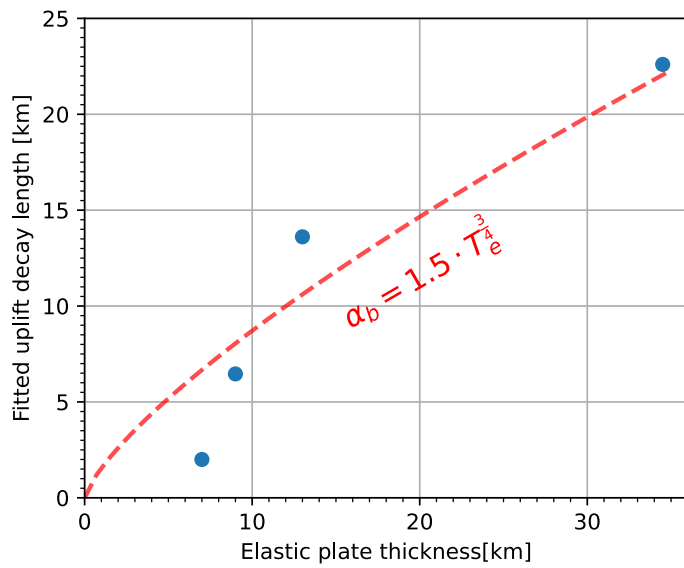
1391

1392

1393 Fig S20 – Fitted wavelength for landscapes. Blue curves show best inverted uplift pattern for
 1394 landscapes. Orange lines show $\alpha \cdot e^{\frac{-x}{b}}$ curves fitted to uplift solutions.

1395

1396



1397
1398
1399 Fig S21 – Fitted equation (2) for landscapes. Blue dots show properties of landscape we used
1400 and red curve show fitted line.
1401
1402
1403
1404
1405
1406
1407
1408
1409
1410

